AD_____

Grant Number DAMD17-96-1-6192

TITLE: Development of High-Resolution Pet Mammogram Modules

PRINCIPAL INVESTIGATOR: Dr. William Worstell

CONTRACTING ORGANIZATION: Boston University
Boston, Massachusetts 02215

REPORT DATE: August 1998

TYPE OF REPORT: Final

PREPARED FOR: U.S. Army Medical Research and Materiel Command
Fort Detrick, Maryland 21702-5012

REPORT DOCUMENTATION PAGE

Form Approved
OMB No. 0704-0188

1. AGENCY USE ONLY *(Leave blank)*	2. REPORT DATE	3. REPORT TYPE AND DATES COVERED
	August 1998	Final (1 Jul 96 - 30 Jun 98)

4. TITLE AND SUBTITLE
Development of High-Resolution Pet Mammogram Modules

5. FUNDING NUMBERS
DAMD17-96-1-6192

6. AUTHOR(S)
Dr. William Worstell

7. PERFORMING ORGANIZATION NAME(S) AND ADDRESS(ES)
Boston University
Boston, Massachusetts 02215

8. PERFORMING ORGANIZATION REPORT NUMBER

9. SPONSORING/MONITORING AGENCY NAME(S) AND ADDRESS(ES)
U.S. Army Medical Research and Materiel Command
Fort Detrick, Maryland 21702-5012

10. SPONSORING/MONITORING AGENCY REPORT NUMBER

11. SUPPLEMENTARY NOTES

12a. DISTRIBUTION / AVAILABILITY STATEMENT
Approved for public release; distribution unlimited

12b. DISTRIBUTION CODE

13. ABSTRACT *(Maximum 200*

Early detection of breast cancer is critical to successful treatment. Unfortunately, conventional x-ray mammography has severe limitations in early tumor detection, in particular for women with radiographically dense breasts. For this reason, nuclear medicine techniques are beginning to be applied to diagnostic breast imaging. Among nuclear medicine techniques, Positron Emission Tomography (PET) has the greatest potential for high sensitivity to small tumors, and good uptake ratios have been demonstrated for breast tumors with the PET radiotracer Fluorodeoxyglucose (FDG). The key PET detector attributes for this application are high acceptance and good efficiency at high rates, fine spatial resolution, and good scatter rejection. We have constructed and tested novel prototype PET detector modules which produce very high-resolution images in all three dimensions, with large acceptance and high rate capability. Our devices exhibited performance in generally good agreement with our expectations, and obtained an intrinsic spatial resolution of better than 3mm FWHM.

We also developed 3-D iterative image reconstruction techniques which have broad application to tomographic breast imaging in nuclear medicine, and for other purposes.

14. SUBJECT TERMS	15. NUMBER OF PAGES
Breast Cancer	53
	16. PRICE CODE

17. SECURITY CLASSIFICATION OF REPORT	18. SECURITY CLASSIFICATION OF THIS PAGE	19. SECURITY CLASSIFICATION OF ABSTRACT	20. LIMITATION OF ABSTRACT
Unclassified	Unclassified	Unclassified	Unlimited

FOREWORD

Opinions, interpretations, conclusions and recommendations are those of the author and are not necessarily endorsed by the U.S. Army.

✓ Where copyrighted material is quoted, permission has been obtained to use such material.

NA ✓ Where material from documents designated for limited distribution is quoted, permission has been obtained to use the material.

✓ Citations of commercial organizations and trade names in this report do not constitute an official Department of Army endorsement or approval of the products or services of these organizations.

NA In conducting research using animals, the investigator(s) adhered to the "Guide for the Care and Use of Laboratory Animals," prepared by the Committee on Care and use of Laboratory Animals of the Institute of Laboratory Resources, national Research Council (NIH Publication No. 86-23, Revised 1985).

✓ For the protection of human subjects, the investigator(s) adhered to policies of applicable Federal Law 45 CFR 46.

NA In conducting research utilizing recombinant DNA technology, the investigator(s) adhered to current guidelines promulgated by the National Institutes of Health.

NA In the conduct of research utilizing recombinant DNA, the investigator(s) adhered to the NIH Guidelines for Research Involving Recombinant DNA Molecules.

NA In the conduct of research involving hazardous organisms, the investigator(s) adhered to the CDC-NIH Guide for Biosafety in Microbiological and Biomedical Laboratories.

10/1/98

PI - Signature Date

TABLE OF CONTENTS:

INTRODUCTION:

The following statement from our 1995 IDEA grant proposal has held up over the intervening 4 years:

"Early detection of breast cancer is critical to successful treatment. Unfortunately, conventional x-ray mammography has severe limitations in early tumor detection, in particular for women with radiographically dense breasts. For this reason, nuclear medicine techniques are beginning to be applied to diagnostic breast imaging. Among nuclear medicine techniques, Positron Emission Tomography (PET) has the greastest potential for high sensitivity to small tumors, and good uptake ratios have been demonstrated for breast tumors with the standard PET radiotracer Fluorodeoxyglucose (FDG). The key PET detector attributes for this application are high acceptance and good efficiency at high rates, fine spatial resolution, and good scatter rejection."

For these reasons, we proposed to construct and test modular components of a novel prototype PET detector module which was to produce very high-resolution images in all three dimensions, with large acceptance and high rate capability. We did build and test such modules, and their performance was in general in reasonably good agreement with expectations. Our original plan was to design modules as parts of a unit to be mounted on a standard mammography stand. The prototype devices as constructed were however not at all ergonomically convenient when deployed on a mammography stand (although we did acquire and mechanically modified a mammography gantry for this purpose), despite our best efforts within our budget. Subsequently, we have continued to work on positron emission mammography through research support from other sources after our US Army grant effort finished, and recently we have developed a system which is much more compact and is compatible with x-ray systems. In what follows we will discuss in detail our experience in the US Army-funded development program which established the feasibility of the detector design which are continuing to carry forward, as well as the important data acquisition electronics and image reconstruction techniques which we developed with (in part) US Army support. The categories below will be reproduced in the Table of Contents and in the Body of this Final Report.

Detector Construction:

We proposed to construct our prototype detector modules using newly-developed LSO (Lutetium OxyorthoSilicate) scintillator crystals read out through wavelength-shifting fiber optics. As it happened, the availability of LSO scintillator was very much more limited than was projected by its sole source (CTI, Inc.) at the time of our proposal. We were eventually able to procure some 100 cc's of this material, and were able to characterize devices built from it with some accuracy. This was much less material that would have been needed to make efficient large-area detectors, however. The sole supplier of LSO subsequently restricted its distribution to "internal use only" within there organization for the next two years. Consequently, much of our subsequent efforts were carried out using CsI(Na) scintillator rather than LSO. While CsI(Na) is readily available and a factor of 10 less expensive than LSO, it is also near 10 times slower and has a smaller photofraction. Nonetheless, it proved quite a reasonable material for our development effort -- somewhat akin to developing a sculpture in wood or plaster before attempting it in marble. Details of our experience constructing these new devices, both at the component and system level, are presented as a narrative in the following section. These results are given at a more detailed level than in the publications which we produced and have enclosed as discussions of other aspects of our US Army-funded research effort. We have a included a quite detailed description in this report both as an indication of the level of effort required and as a guide to others who might seek to follow in our footsteps -- in particular to alert them to the pitfalls into which we on occasion fell.

Optoelectronics and Data Acquisition Electronics:

Details of our work characterizing and selecting an appropriate multianode photomultiplier system for wavelength-shifting fiber readout are given in a Conference Proceeding which follows ("Characterization of a new multianode PMT for low-level optical fiber readout"). One aspect of our system which required considerably more time and effort than originally estimated was the development of high-rate portable data acquisition electronics. The final system which we developed is discussed in a recent submission to IEEE Transactions in Nuclear Science ("A 500K Event/Sec 12-Bit ADC System with High-Speed Buffered PCI Interface").

Detector Performance:

Details of our detector system performance are given in a Conference Proceeding ("Development of a High-Resolution PET Detector using LSO and Wavelength-Shifting Fibers" and a publication which has been accepted in a refereed journal ("First Results with High-Resolution PET Detector Modules using Wavelength-Shifting Fibers" in IEEE Transactions in Medical Imaging.) The intrinsic spatial resolution was not as precise as had been originally hoped (1-2mm FWHM), principally because the contribution to resolution blurring from Compton scattering within the detectors was underestimated in our original estimates of anticipated device performance. The best we were able to achieve in practice was 2-3mm FWHM. Furthermore, at this level of performance intrinsic spatial resolution is significantly less important than high efficiency, large acceptance, and high rate capability. Because of the limited activity which can be delivered to the patient, and because of the limited sensitivity of even with a very efficient detector with relatively high protofraction (fraction of most usable events) in close proximity to the breast (very large acceptance), accurate detection and quantitation of very small lesions is limited by event statistics rather than intrinsic resolution for a device with <3mm FWHM resolution.

Image Reconstruction:

In the process of developing image reconstruction techniques for use with our novel breast imaging detector, we serendipitously stumbled upon a very promising 3D iterative image reconstruction method using Monte Carlo methods. This "Inverse Monte Carlo" or "Monte Carlo System Response sampling" techniques has turned out to a representative of an entire class of procedures for implementing "standard" 3D iterative reconstruction algorithms without requiring explicit calculation of the system response matrix. This system response matrix is so large that even when allowing for symmetries and zero-suppressing to allow for its sparseness, it is impractical to store it explicitly even on disk, much less in computer memory. Our "Inverse Monte Carlo" reconstruction technique is therefore of quite general importance, and particularly of interest for breast imaging because of the required detector acquisition geometry in this case. One Conference Proceeding ("An Inverse Monte Carlo Algorithm for 3-D PET Reconstruction") and extended abstracts which have submitted to a future conference ("Quantitative Evaluation of an Inverse Monte Carlo procedure for 3-D PET Image Reconstruction" and "3-D Iterative Reconstruction Procedures for PET Detectors with Fixed Dual-Plane Geometry").

Future Directions:

As noted earlier, we have obtained support for follow-on efforts and remain committed to developing instrumentation for Positron Emission Mammography (PEM) , both using the detector design whose development was supported by this grant, and using other detector designs which are more compatible with x-ray mammography gantries. The fiber-based design which this effort helped to develop is more cost-effective for large-area application and gives important depth-of-interaction effort, while our newer more compact design is more x-ray compatible. We may in fact meld the two designs at some future juncture. The 3-D iterative reconstruction techniques which this effort helped us to develop have wide application for PEM and in fact to 3-D PET generally.

DETECTOR CONSTRUCTION

The details of our detector design have evolved through several iterations of a construction/test cycle, and have been informed by a variety of component-level tests and computer simulations. Principle component-level test and development results are indicated below.

1) Crystal geometry and surface preparation:

Our crystal geometry of 112mm x 112mm x 2.5mm was based upon readout through 8 ribbons each on the x- and y- surfaces of each crystal, where each ribbon is 14mm across. This 14mm number arose from measurements on early production units of the Hamamatsu R5900-L16 position-sensitive photomultipliers which we use to read out the fibers. The 2.5mm thickness was based on a target resolution of 2.0mm FWHM (Full Width at Half Maximum), which we expect to be a good match to the statistical limits in image quality available for a high-efficiency PET mammography unit for anticipated clinical doses and scan times. The quality of the scintillator crystal surface finish is important in our application for two reasons: first, because we require a clear division between light which is totally internally reflected within the crystal and that light which emerges from the crystal into the fiber ribbons (for good spatial resolution), and second because we need the overall crystal/fiber laminated stack to be transparent to wavelength-shifted light (for good energy resolution). We require such transparency because in our device we have separated the functions of interaction position measurement (through the fiber readout) from gamma ray energy measurement and triggering/timing (through an Anger array of photomultipliers which view each stack). Because both the scintillator crystals and the fibers are transparent to the wavelength-shifted light, photons traversing the wide range of optical indices within the stack are scattered rather than absorbed; small scratches on the crystal surface from imperfect polishing, however, absorb light and can cause excessive attenuation of wavelength-shifted light within the laminate. In our devices, we surround the laminated stack by reflective material on all sides except that side with the Anger array, and we are able to obtain good energy and timing resolution as well as good uniformity of response. Because CsI(Na) does not readily polish to an optical finish and because it is somewhat hygroscopic, considerable effort was needed in order to obtain an adequate surface finish (using silicon oil and progressively smaller sizes of Aluminum Oxide powder abrasives). Our final procedure yielded less than 10-20% variation in light collection from one side of the stack versus the other, which is readily corrected since the depth of interaction in the stack is measured.

The effect of imperfect surface preparationof CsI(Na) on spatial resolution was difficult to analyze, and measurement of the amount of scintillation light scattering from crystal surface imperfections (rather than totally internally reflecting) required a great deal of experimentation. Finally, we were able to determine that our imaging resolution for 2.5mm thick plates of CsI(Na) is limited by Compton scattering and secondary photon capture within a single plate. The true photofraction (ratio of photocapture events to all gamma-ray interactions) for 511 keV gamma rays in CsI(Na) is about 15%, while the apparent photofraction (fraction of events within the photopeak for 511 keV gammas normally incident on a 2.5mm thick plate) is more than 25%. The difference arises from gammas which Compton scatter at 90 degrees, followed by photocapture of the secondary gamma rays. These secondary gammas have energies near 250 keV and a range of about 7 mm in CsI(Na); computer simulations show a limiting resolution due to this effect close to our observed 2.5mm FWHM, for two detectors in coincidence. For a CsI(Na) device, this effect can be somewhat lessened with thinner crystals, which increases the fraction of "true" photocaptures within "apparent" photocaptures (by decreasing the angular acceptance for secondaries to convert in the same crystal) but this either increases the number of detector layers required or decreases the overall efficiency.

2) Optical coupling of crystals to fibers:

Our second round of prototype modules (the first had attenuation difficulties due to imperfect crystal surface treatment) yielded a significantly lower fiber light yield relative to the first, for reasons which were not understood at first. After some experimentation, we discovered that the effect was due to a relatively high-index optical epoxy which we used to coat the hygroscopic crystals; once we determined that the crystals did not degrade with ambient humidity over a time scale of 1-2 weeks (the time between cutting/polishing and sealing them into laminated modules) we omitted the coating step. Although the crystals did not degrade, the greater optical index mismatch without the coating trapped more light within the crystal and decreased our fiber light yield. In the third round of prototypes, the light yield was restored and slightly improved by introducing a crystal coating layer with refractive index near the geometric mean between that of the crystal and that of the fiber outer cladding; this thin layer then serves as an antireflection coating.

3) Fiber selection and preparation:

We experimented with both round and square cross-section fibers, with different fluor formulations and concentrations, and with diameters ranging from 0.5mm to 1.0mm. Round fibers gave nearly a factor of two better light yield relative to square fibers, which is due to much smaller attenuation losses along the fibers with round cross-sections. This arises because the square fibers do not have a precisely square cross-section, leading to optical ray paths which encounter the core/cladding interface at more than the critical glancing incidence angle. Similarly, 1mm fibers have significantly higher light yield than 0.5mm fibers, in this case due to self-absorption to the limited Stokes shift between absorption and emission, combined with the higher fluor concentrations required for efficienct fluorescent in 0.5mm fibers. We have used multi-clad fibers and succeeded in obtaining 50% light yield improvements by optically coupling aluminized mylar mirrors to the ends of polished fiber ribbons. This is used to obtain two active edges and an active corner opposite the readout ends of the fibers.

4) Multilayer stack assembly and fixing:

Multilayer crystal/fiber stacks were built up from acrylic "frames" 3.5mm thick, with cutaway regions on one side to guide a 1mm thickness fiber ribbon, and a square opening in the center to position the 112mm x 112mm coated crystal. Fiber ribbons are first glued to frames, then a stack is built up by placing coated crystals onto fibers within each frame, with the axes of the fiber ribbons alternating between two orientations as the stack was built up. We devoted considerable effort to developing procedures for casting the modules with a potting epoxy, so as to fill all interstices without generating air gaps or bubbles; we ultimately succeeded in casting nearly defect-free 7-crystal-deep stacks. Wavelength-shifting fibers were also coupled to the perimeter of each crystal in a stack, with these fibers read out separately to determine the depth-of-interaction within a stack (these fibers detected the light which was trapped in a crystal layer and guided to the perimeter through total internal reflection). We obtained a light yield of about 10 photoelectrons for 0.5mm diameter perimeter fibers, which is more than sufficient to determine depth-of-interaction to within the crystal thickness of 2.5mm. The top of each module was epoxied to a 2.5cm-thick "light mixer" coupled to four 2" diameter photomultipliers in an Anger array. The bottom of each module was optically coupled to reflecting material after assembly, as were the edges of the light mixer and those regions of the light mixer not covered by Anger PMTs. Fiber ends which were not read out were polished and optically coupled to aluminized mylar mirrors. The resulting modules have two "active edges" and an "active corner", reflecting the desire of our clinical colleagues for a device which could be used to image near the chest wall for breast imaging and well up into the armpit for axillary imaging.

5) Fiber ribbon routing, multiplexing, and readout coupling:

Our initial tests used multiplexed readout of two ribbons per multianode photomultiplier, where a rough coordinate from the Anger PMT array was used to demultiplex between the two ribbons on each fiber readout PMT (i.e. "lateral" multiplexing within a single-crystal-layer device). There is sufficient photocathode area on our multianode photomultipliers to permit both 4-fold lateral multiplexing and 4-fold multiplexing in depth when using 1mm diameter fibers, but such heavy multiplexing will not in future be needed because of the new multianode photomultiplier options discussed in the next section. Given the significant price of each multianode photomultiplier it is important to keep their numbers down, but heavy multiplexing decreases system rate capability by introducing pile-up and demultiplexing errors at high event rates. The higher rate capability with new multianode photomultipliers is desirable, but will require an increase in data acquisition electronics channel count. In all cases, fibers were optically coupled to multianode PMTs by inserting fiber ribbons into custom-built vises, polishing the fiber ends, then optically coupling to the PMTs by attaching the vises to custom PMT mounting mechanics.

6) Multianode photomultipliers and associated electronics:

We used Hamamatsu R5900-L16 multianode photomultipliers to read out the fibers, where each multianode PMT contained 16 separate photocathode regions each 16mm x 1mm. The 16 anodes were resistively coupled in a chain and read out through charge division. We were able to obtain spatial resolution of less than 1mm FWHM for 8 photoelectrons incident through a single 1mm fiber; our spatial resolution is therefore not limited by our PMT readout, but rather by upstream optics. The two charge-division outputs (whose ratio give the transverse coordinate for light incident through a fiber ribbon, and whose sum gives the total fiber light yield) were read out through custom-built 4-PMT bases and coupled to x10 preamplifiers which we also constructed. The single photoelectron peak from the multianode photomultipliers was very pronounced, simplifying detector gain calibration considerably.

7) Coincidence trigger:

We used commercial NIM electronics to construct a simple but adequate trigger for our system. It begins with an analog fan-in/fan-out module which combines the four Anger PMT signals (which are split in two by 50-ohm splitters, with the second half going to ADCs) to make a single signal from each module; these signals are then discriminated, and a trigger resulting from a coincidence between the two discriminated signals generates a gate which initiates ADC conversion and later event readout. We have assembled a second commercial NIM trigger subsystem as part of the portable system we are building.

8) Data acquisition electronics and computer interface:

We used commercial LeCroy 2249W ADCs to digitize the outputs of both 4 Anger PMTs per module and 16 multianode PMT charge-division outputs per module. A trigger was generated from the coincidence of discriminated output of analog-summed Anger PMT signals, and each of the 40 digitized signals was delayed by 200ns to land within a 1000ns-width gate. A second, lower threshold was also set on each Anger PMT sum, and the outputs of these discriminators sent to a LeCroy 2228 TDC to determine the coincidence time resolution as a function of threshold. CAMAC readout of the 42 detector channels was performed with a crate controller designed at the Budker Institute for Nuclear Physics in Siberia, which is capable of nearly 10KHz readout of this many channels and is coupled to a PC. In addition to the 2249W ADC system we have tested a few modules of FERA-Fast Encoding and Readout ADCs. These zero-suppressing and fast conversion-time modules should extend our system rate capability to 50-100 Khz, which is a higher rate than we expect at reasonable patient doses.

Figure 13: Drawing #10 -- Conceptual drawing of two proposed detector modules mounted on mammograph -- note that actual mammograph (unlike unit shown) has a detachable bucky/cartridge support structure.

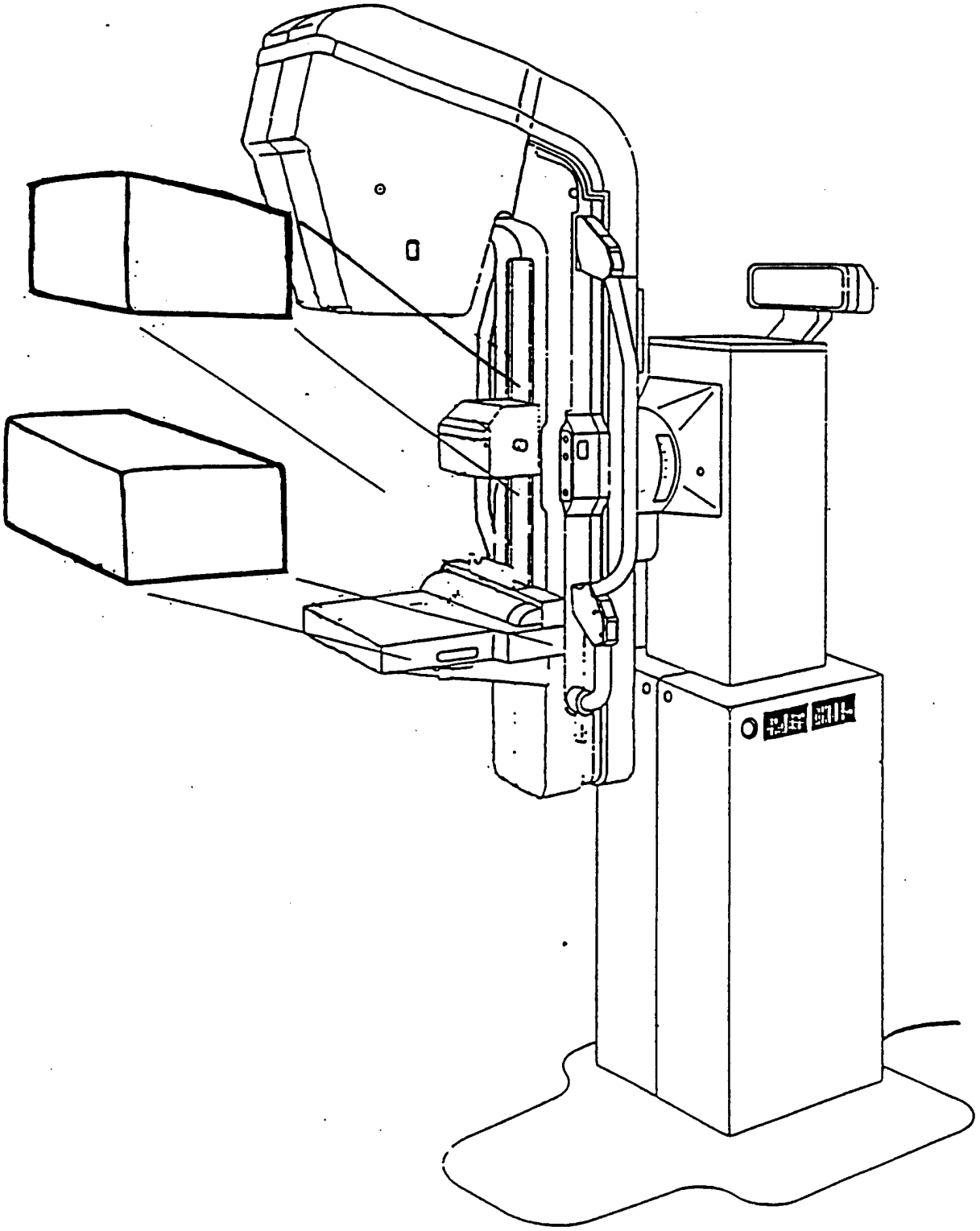

Rev	Description	Date
A	CREATED DRAWING	06-10-07

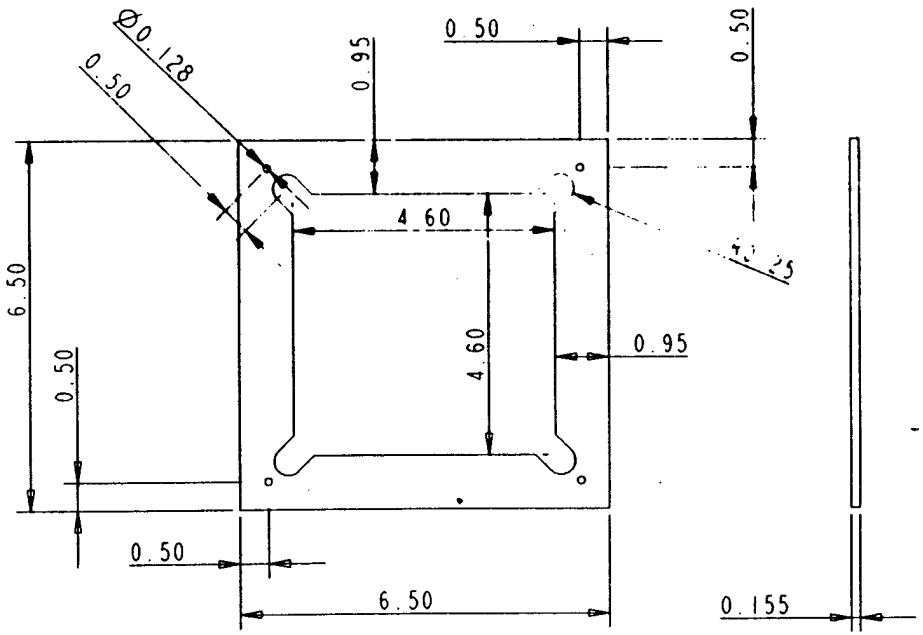

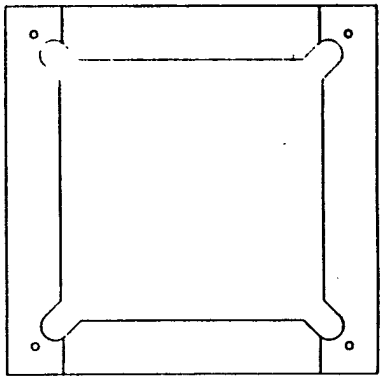

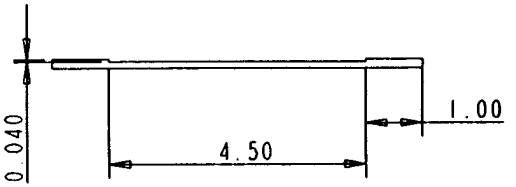

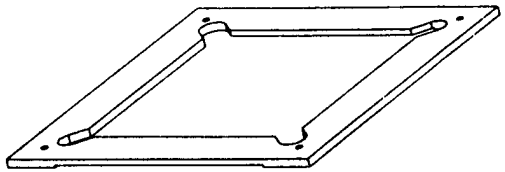

10 PCS

FINISH: AS MACHINED		[redacted]	
UNLESS OTHERWISE NOTED, BREAK ALL SHARP EDGES & CORNERS	SHEET 1 OF 1	FRAME, RIBBON SLOT ONLY	
STATUS	DATE	DWG# RR-0013	REV: A Size: B
DRAWN: K. RITSHER	06-10-07	SCALE: 0.500	MAT'L: CLEAR [illegible]
		Unless otherwise noted, dimensions are in inches .XX=± 02 XXX=± 003 DEGREES=±1/2° DO NOT SCALE PRINT	
DRAWING FRAME_W_RIBBON_ONLY MODEL: FRAME3			

Rev	Description	Date
A	CREATED DRAWING	08-10-97

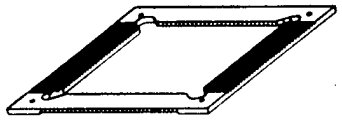

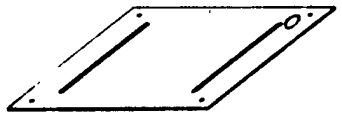

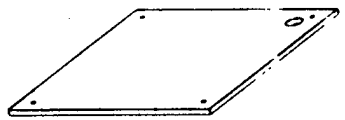

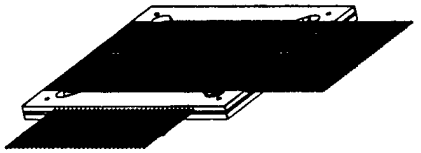

FINISH SEE NOTES		[illegible]		
UNLESS OTHERWISE NOTED, BREAK ALL SHARP EDGES & CORNERS	SHEET 1 OF 1	PARTIAL STACK ASSEMBLY		
STATUS	DATE	DWG# xxx-xxx-xxx	REV A	Size: B
DRAWN R RITSHER	08-10-97	SCALE: 0.333	MAT'L SEE NOTES	
		Unless otherwise noted, dimensions are in inches		
DRAWING STACK_ASSY MODEL STACK		XX=± 02 .XXX=± 003 DEGREES=±1/2° DO NOT SCALE PRINT		

Rev	Description	Date
A	CREATED DRAWING	05-10-97

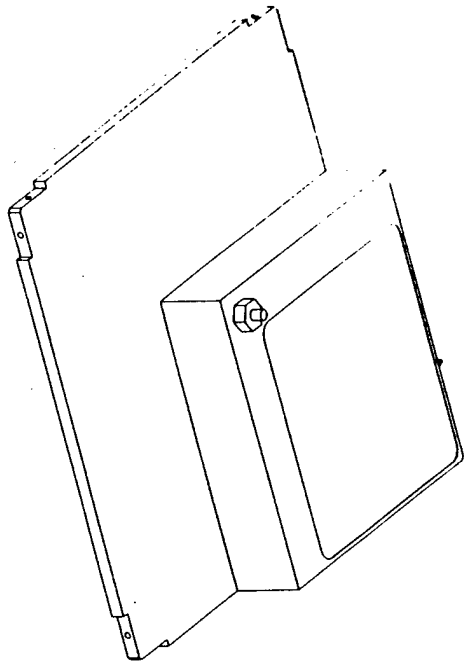

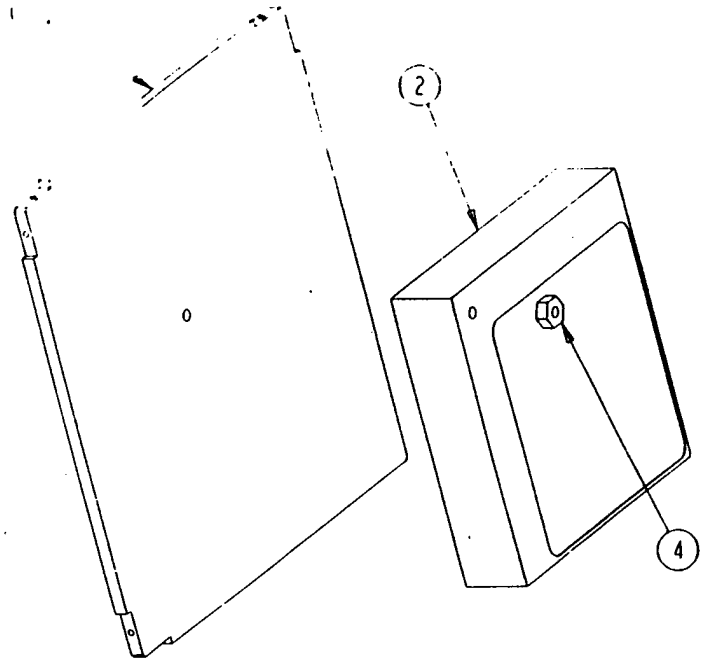

1. 10-32 X 2" FLAT HEAD MACHINE SCREW
2. BASE PLATE BU-0002
3. TRIMMED STACK ASSY BU-0008 (FIBERS NOT SHOWN)
4. 10-32 NUT

FINISH: SEE NOTES		[illegible]	
UNLESS OTHERWISE NOTED, BREAK ALL SHARP EDGES & CORNERS	SHEET 1 OF 1	BASE PLATE STACK ASSY (STEP ONE)	
STATUS	DATE	DWG# BU-0001-A	REV: A Size: B
DRAWN: R. RITSHER	05-10-97	SCALE: 0.500	MAT'L: SEE NOTES
		Unless otherwise noted, dimensions are in inches	
DRAWING BU-0001-A MODEL PNT.ASSY		XX:± 02 XXX:± 003 DEGREES:±1/2° DO NOT SCALE PRINT	

Rev	Description	Date
B	REDUCED HEIGHT	6-19-97

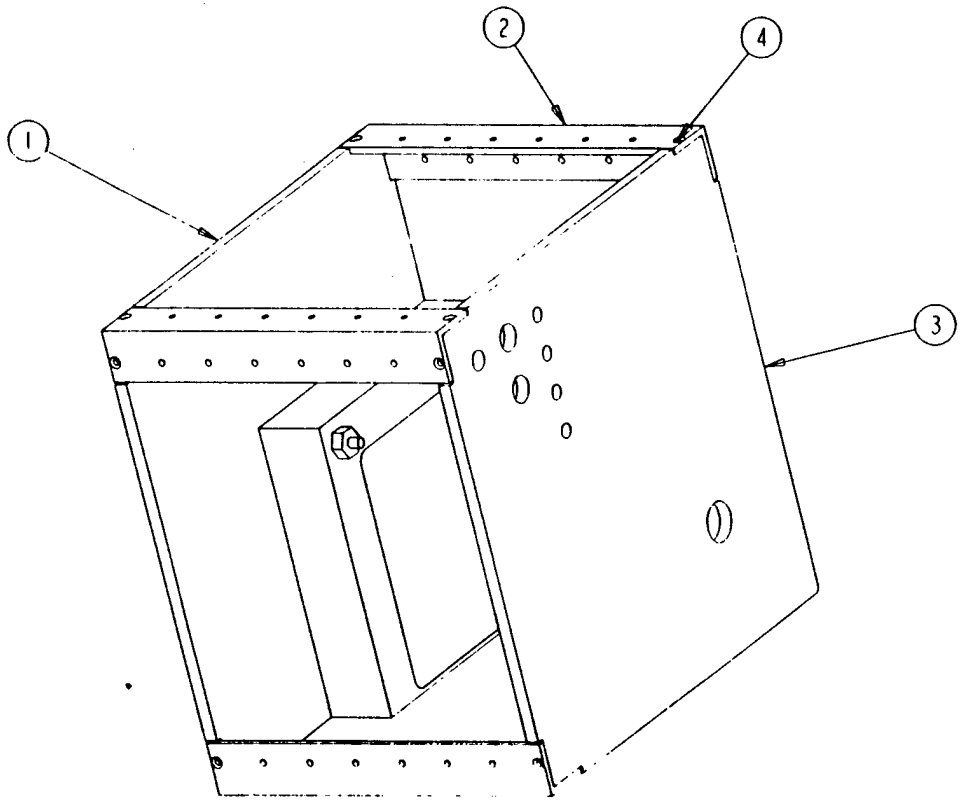

1 BASE PLATE STACK SUB-ASSY BU-0001-A
2 ANGLE BRACKET BU-0001 QTY 3
3 TOP PLATE BU-0007
4 4-40 X 3/8 FLAT HEAD MACHINE SCREW QTY 12

FINISH SEE NOTES		KEN RITSHER 10 JEWETT ST SHATTUCK MA 02172 617-624-6234	
UNLESS OTHERWISE NOTED, BREAK ALL SHARP EDGES & CORNERS	SHEET 1 OF 1	FRAME ASSEMBLY	
STATUS	DATE	DWG# BU-0002-A	REV B / Size B
DRAWN K RITSHER	05-10-97	SCALE: 0.500	MAT'L SEE NOTES
		Unless otherwise noted, dimensions are in inches	
DRAWING BU-0002-A MODEL PMT_ASSY		XX:± .02 XXX:± .003 DEGREES:±1/2° DO NOT SCALE PRINT	

Rev	Description	Date
B	REDUCED HEIGHT	06-19-97

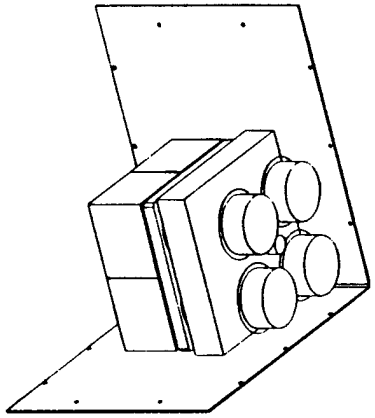

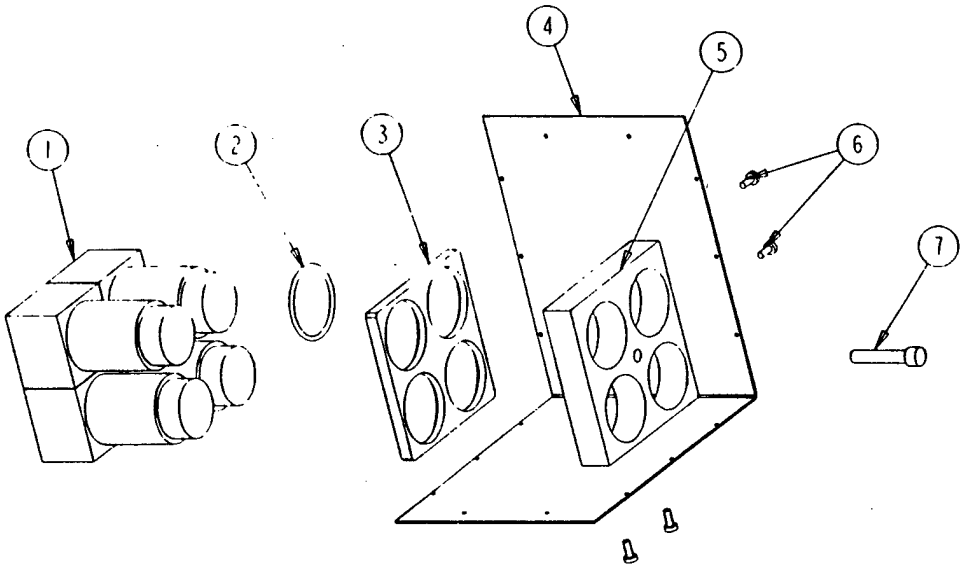

1 PMT QTY 4
2 226 ORING QTY 4 (1 SHOWN)
3 PRESSURE PLATE BU 0003
4 ANGLED CHANNEL BU 0005
5 SCREW PLATE BU 0004
6 10-32 X 1/2" PAN HEAD MACHINE SCREW QTY 4
7 3/8 16 X [illegible]

FINISH SEE NOTES		KEN RITSHER 10 JEWETT ST WATERTOWN MA 02172 617-924-6234
UNLESS OTHERWISE NOTED, BREAK ALL SHARP EDGES & CORNERS	SHEET 1 OF 1	PMT ASSEMBLY
STATUS	DATE	DWG# BU 0004 A / REV B / Size B
DRAWN K RITSHER	05 10-97	SCALE 0 300 / MAT'L SEE NOTES
DRAWING BU 0004 A MODEL PMT_ASSY		Unless otherwise noted, dimensions are in inches XX:± 02 XXX:± 003 DEGREES:±1/2° DO NOT SCALE PRINT

Rev	Description	Date
B	REDUCED HEIGHT	06-19-97

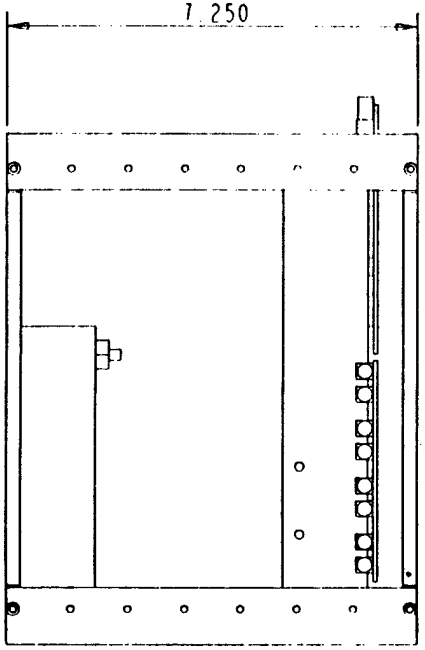

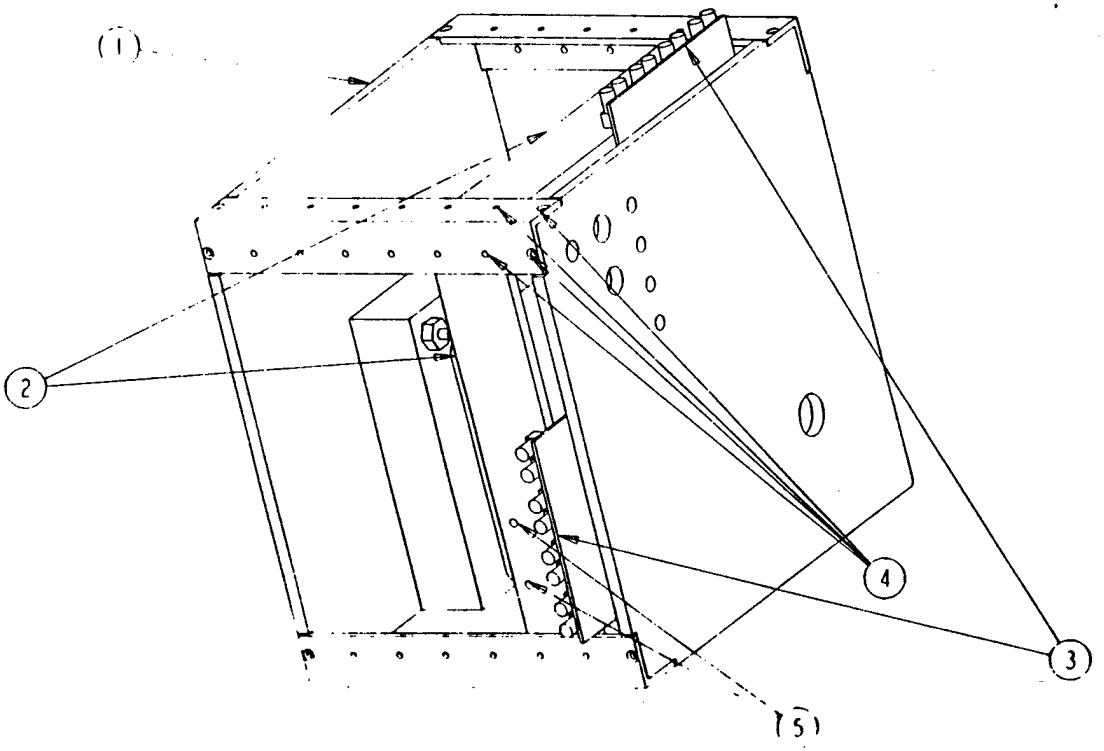

1 FRAME ASSEMBLY BU 0002 A
2 STRUT BU 0006 QTY 2
3 PCB/FIBER ASSEMBLY QTY 2
4 4-40 X 3/8" SHCS QTY 8 (FROM INSIDE)
5 6-32 X 1/2" PAN HEAD MACHINE SCREW QTY 4

FINISH SEE NOTES		KEN RITSHER 10 JEWETT ST WATERTOWN MA 02172 617-924-9224
UNLESS OTHERWISE NOTED, BREAK ALL SHARP EDGES & CORNERS	SHEET 1 OF 1	PCB ASSEMBLY
STATUS	DATE	DWG# BU 0003 A / REV B / Size B
DRAWN K RITSHER	05-10-97	SCALE 0.500 / MAT'L SEE NOTES
DRAWING BU 0003-A MODEL PWT.ASSY		Unless otherwise noted, dimensions are in inches XX:± .02 XXX:± .003 DEGREES:±1/2° DO NOT SCALE PRINT

Rev	Description	Date
A	CREATED DRAWING	06-19-97

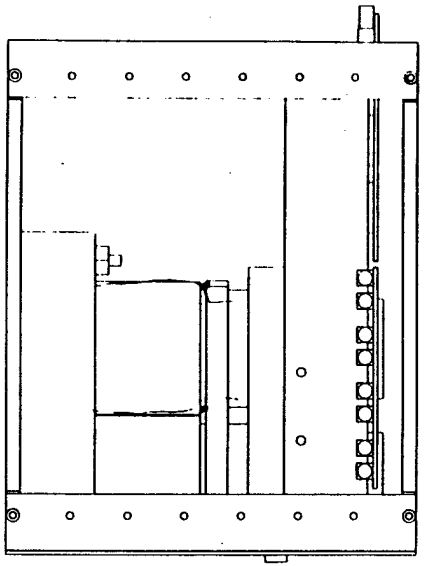

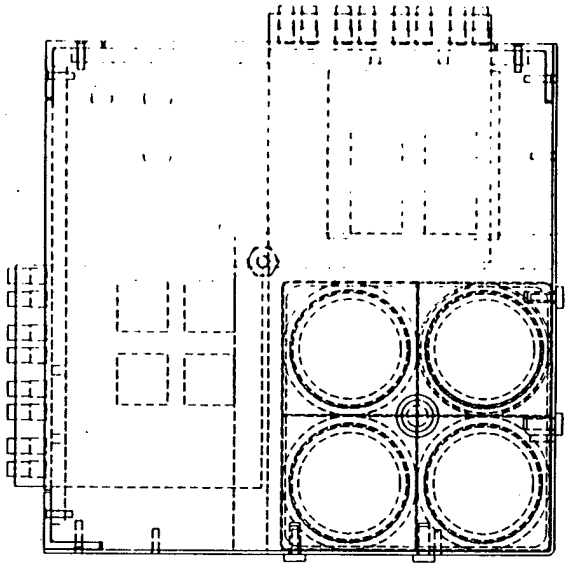

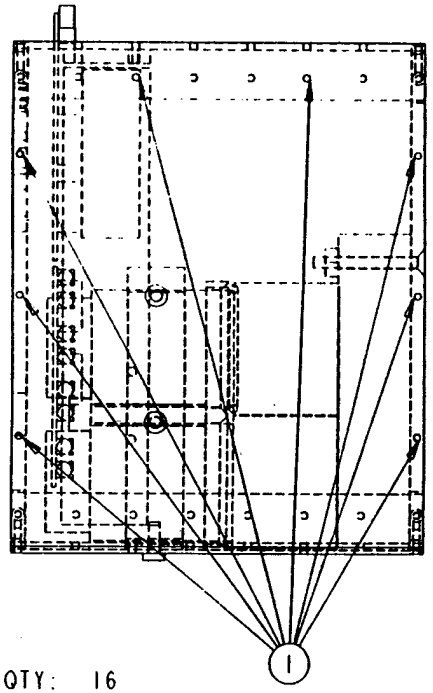

1 4-40 X 3/8 SHCS QTY: 16

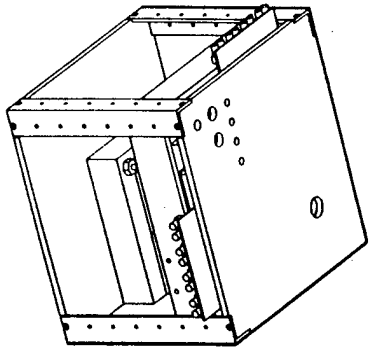

SCALE 0.250

FINISH: SEE NOTES		[illegible]
UNLESS OTHERWISE NOTED, BREAK ALL SHARP EDGES & CORNERS	SHEET 1 OF 1	ASSEMBLY: PMT S.A. TO CHASSIS S.A.
STATUS	DATE	DWG# BU-0005-A / REV: A / Size: B
DRAWN: K RITSHER	06-19-97	SCALE: 0.500 / MAT'L: SEE NOTES
		Unless otherwise noted, dimensions are in inches XX:± 02 XXX:± 003 DEGREES:±1/2° DO NOT SCALE PRINT
DRAWING BU-0005-A MODEL PMT_ASSY		

Rev	Description	Date
A	CREATED DRAWING	07-15-97

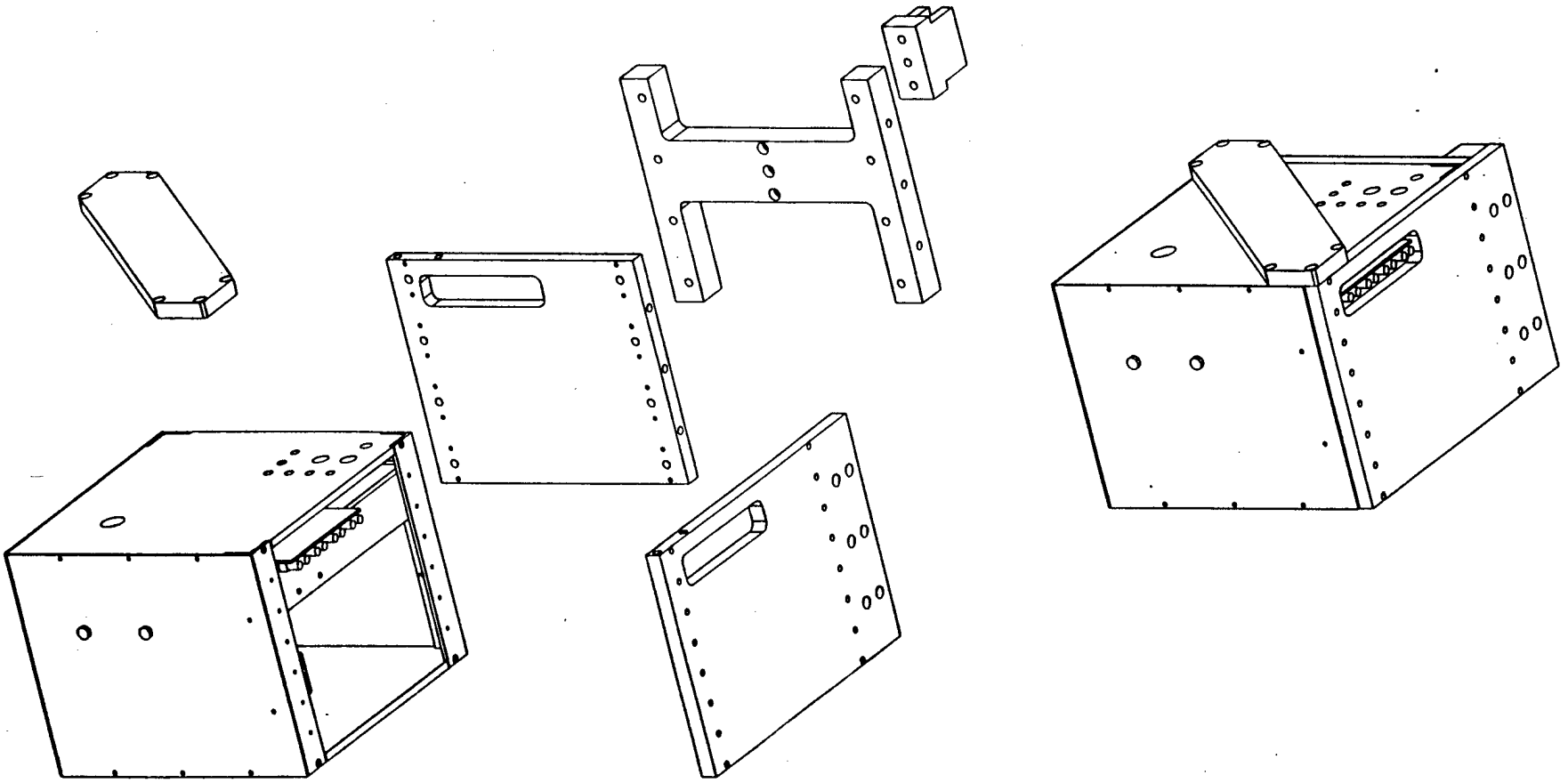

FINISH SEE NOTES		NEW JERSEY ID JERSEY ST WATERTOWN MA 02172 617-924-6284
UNLESS OTHERWISE NOTED, BREAK ALL SHARP EDGES & CORNERS	SHEET 1 OF 1	TOP ASSEMBLY
STATUS	DATE	DWG# xxx-xxx-xxx / REV: A / Size: B
DRAWN: K. RITSHER	07-15-97	SCALE: 0.333 / MAT'L: SEE NOTES
		Unless otherwise noted, dimensions are in inches .XX=±.02 .XXX=± 003 DEGREES=±1/2° DO NOT SCALE PRINT
DRAWING: TOP_BRACKET MODEL: BRACKET		

Rev	Description	Date
A	CREATED DRAWING	07-15-97

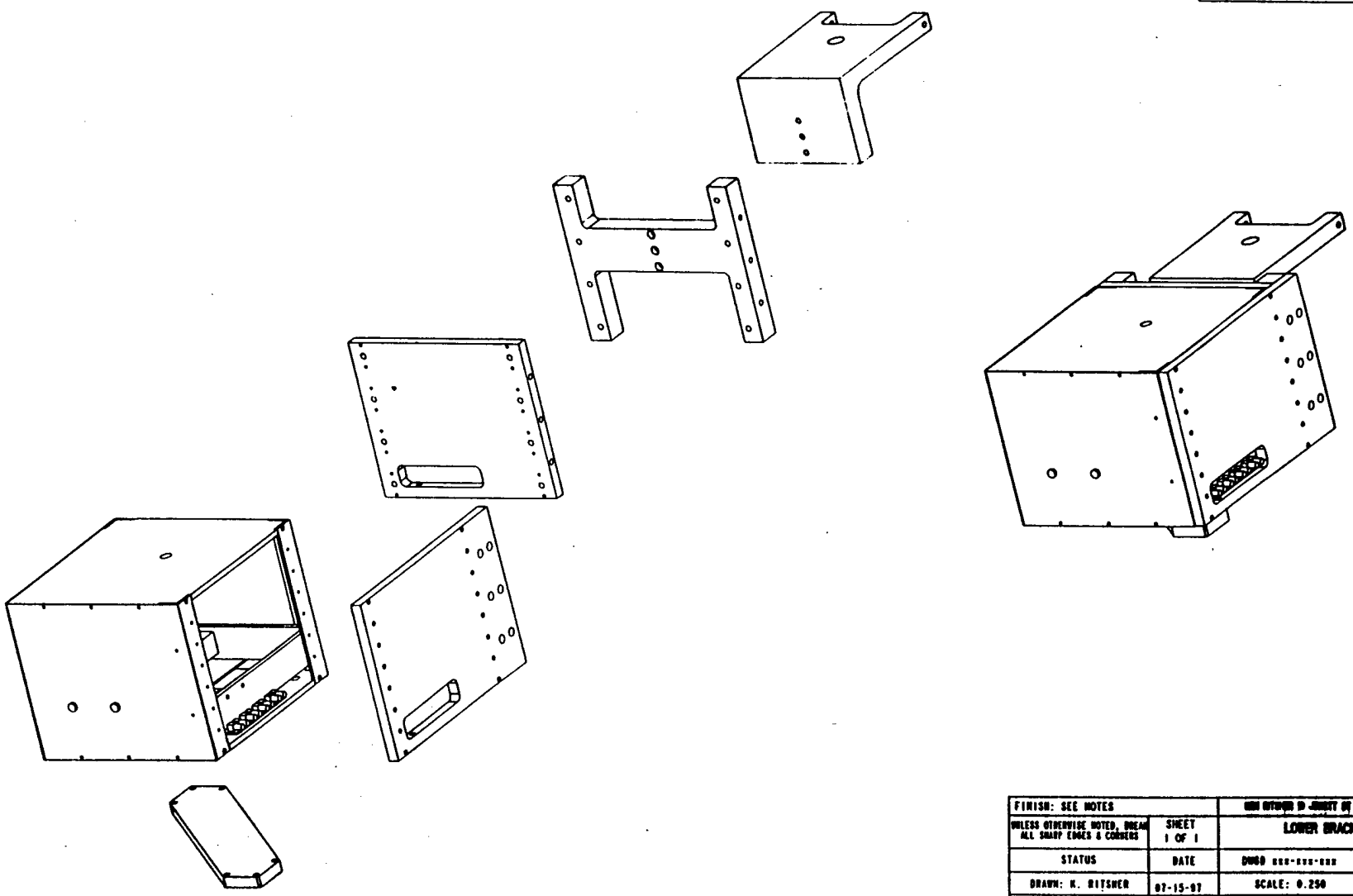

FINISH: SEE NOTES		[illegible]	
UNLESS OTHERWISE NOTED, BREAK ALL SHARP EDGES & CORNERS	SHEET 1 OF 1	LOWER BRACKET ASSEMBLY	
STATUS	DATE	DWG# xxx-xxx-xxx	REV: A Size: B
DRAWN: K. RITSHER	07-15-97	SCALE: 0.250	MAT'L: SEE NOTES
		Unless otherwise noted, dimensions are in inches .XX=±.02 .XXX=±.003 DEGREES=±1/2° DO NOT SCALE PRINT	
DRAWING: BOTTOM_BRACKET MODEL: BOTTOM_BRACKET			

Characterization of a new multianode PMT for low-level optical fiber readout*

D .Grigoriev [1], O .Johnson[2], W. Worstell[2], V. Zavarzin[3]

[1]Budker Institute of Nuclear Physics, pr. Lavrentieva 11, Novosibirsk 630090, Russia

[2]Boston University Department of Physics, 590 Commonwealth av., Boston MA 02215

[3]Budker Institute of nuclear physics, Novosibirsk, Russia, currently at Boston University

Abstract

We have characterized the new Hamamatsu R5900-L16 multianode photomultiplier with regard to its suitability for position-sensitive readout with just two analog channels for each 16-anode PMT. Because of the low capacitance of the anode structure of the PMT, we obtain an output pulse width of less than 20 ns for narrow input pulses. We were able to obtain position-sensitive readout of single photoelectron pulses with a spatial width of less than 1 mm FWHM for a collimated light source and about 2 mm FWHM for single fiber. Combined with the good single photoelectron peak for R5900-L16, this provides excellent performance at very low light levels. We discuss application of this device to the precise determination of gamma-ray interaction position within thin crystal scintillators.

I. Introduction

Position sensitive photomultipliers have been used by a number of groups for the readout of scintillating or wavelength-shifting fibers. Crossed-wire and multianode PMTs have also been used for the position-sensitive readout of extended light sources [2-5]. At low light levels, the cross-talks within the PMT can result in significant degradation in spatial resolution. There are several sources of such cross-talks: light spreading through the entry window glass on the way to the photocathode, imperfect electron optics between photocathode and dynode structure, secondary electron shower spreading within the multiplier assembly, or just electrical cross-talks between anodes (induced signals). A significant difference between position-sensitive cross-wired PMTs like the Hamamatsu R2486, versus multianode PMTs like the Hamamatsu R4760, is the considerably higher cross-talks and therefore decreased spatial resolution at low light level of the former. The Hamamatsu R2486 for instance requires 10000 photons at 490 nm (about 1000 photoelectrons) to obtain a spatial resolution of 0.2 mm FWHM [2]; the resolution is proportional to the square root of the number of photoelectron per event. Another difficulty with cross-wired PMTs for some applications is its limited rate capability due to significant pulse width with typical resistor chain readout.

Nonetheless, the reduced electronics channel count and lower device cost (particularly per unit of useful photocathode area) associated with crossed-wire PMTs have made them attractive for several applications, including for the readout of sets of scintillating fibers.

There is some success in attempts to use charge division method for two-dimensional readout of an array of optical fibers by multianode PMT having just four analog channels [5]. But again, one needs hundreds of photons to obtain submillimeter resolution.

We investigated the properties of the newly developed PMT - the Hamamatsu R5900-L16 - because of its very promising specifications caused mainly by recently developed microchannel dynode structure.

II. Experimental Setup

A. *R5900-L16 - multianode PMT*

The photomultiplier described here has external dimensions of merely a cube 25*25*25 mm. It has flat bialkali photocathode, 10-stage dynode structure and 16 anode stripes 0.8 * 16 mm regularly spaced at 1 mm pitch. An important feature of the PMT distinguishing it from previous ones is that the microchannel dynodes work effectively like separate PMTs in terms of electron optics. This minimizes electron shower smearing and allows one to obtain very fine spatial resolution as will be shown below. Another useful feature of the microchannel structure is a relatively high gain at low operating voltage - about $3..4*10^6$ at 800V . The first prototype of R5900-L16 sent to us by Hamamatsu had a size of photocathode of 15.5 * 15.5 mm which is a 0.5mm narrower than dynode structure. Most of the measurements were done on this particular PMT. The photocathode size of the last version of R5900-L16 is significantly larger - approximately 21 * 22 mm. We have repeated some of the measurements to check the impact of this design change on the performance.

B. *Charge Division Readout*

We have connected 16 anodes of the PMT by a linear array of 15 100-ohm resistors to couple 16 individual outputs into 2 charge division outputs. Each of the two signals was directly coupled through 50-ohm cables to a LeCroy 2249W operating with a 150 ns gate width. To minimize artifacts caused by discrete nature of ADC data we have inserted 10-fold

*This work was supported through the Boston University Center for Photonics Research, under Grant No. 00014-93-1186 from the Office of Naval Research.

0-7803-3534-1/97 10.00©1997IEEE

amplification of the charge division signals giving us a single photoelectron peak at about 35 channels of the ADC over the pedestal.

B. *Data Acquisition System*

For measurements described here we used rather simple data acquisition system consisting of a CAMAC ADC mentioned above and micro-VAX computer under Open VMS connected to the CAMAC crate and controller via SCSI-bus. Data collected on a disk of the computer then were analyzed in a PAW (CERN written data analysis software) session.

III. Tests and Measurements

A. *Timing and Single Photoelectron Characteristics*

The PMT itself (when its anodes are read out separately) has fast rise time and narrow pulse width - 0.6 ns rise time, 1.7 ns fall time when loaded to 50 Ohm. After connecting all anodes by a linear array of 100-Ohm resistors, we obtain a pulse width of less than 20 ns. To check single photoelectron amplitude peak we connected together two ends of the charge division chain. The PMT was illuminated by a green LED giving 0.1 photoelectron in average. The distribution is shown on Fig. 1. The peak-to-valley ratio of almost 3:1 is a very desirable characteristic for low light level applications.

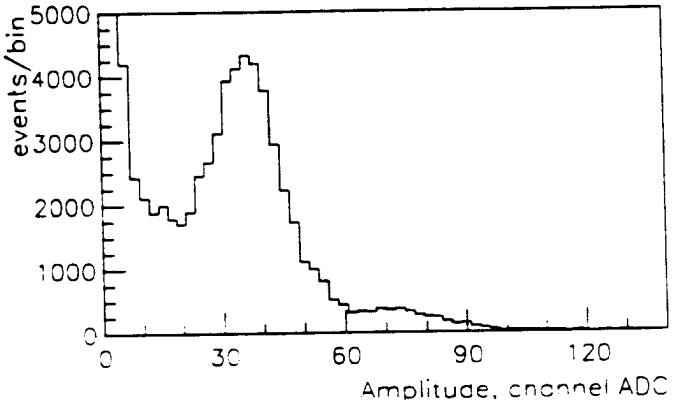

Figure 1: Single photoelectron peak of the R5900-L16. All anodes are read out together. HV=800V.

B. *Charge Division Calibration*

Ideally, if we know parameters of the chain - we can calculate the calibration coefficient between charge division ratio R=(A2-A1)/(A1+A1) (A1 and A2 - amplitudes measured from two ends of the chain) and position in the chain, considering each anode to be a current source. The correspondence between charge division node number and measured ratio R should be linear. Therefore even if several photoelectrons are distributed over several PMT anodes the measured ratio R would correspond to the center-of-gravity of received photoelectrons. In our particular case we have Rin=50 Ohm and 15 resistor of the chain 100 Ohm each. So ideally for point source from the first or the last anode we should measure the ratio

R=+-(50+15*100-50)/(50+15*100+50)=+-0.9375.

In real situation one has to correct this ratio for different gains and input impedances of the two amplifiers. Practically we found that the ratio R ranges from -1.05 to 1.05, which means that anodes others than illuminated by light source produce induced signals of inverse polarity. Indeed we have seen and measured such signals on the scope - the sum of all anodes but illuminated one gives approximately 15% of the main signal. Neglecting the fact of induced signals we could calculate the linear coefficient for conversion of the measured ratio R to the signal center-of-gravity position:

K=15/(1.05-(-1.05))=7.14,

where 15mm - separation between the first and the last anodes. Using this coefficient we have plotted then center-of-gravity coordinate versus actual position of the light source. The plot and linear fit of the data are shown on Fig.2.

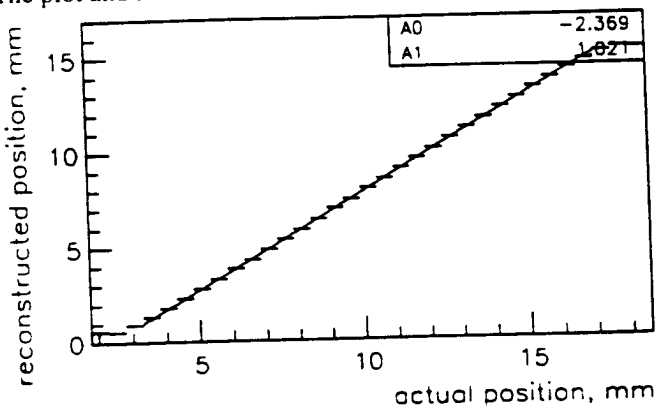

Figure 2: Reconstructed coordinate linearity. A 0.5 mm fiber coupled to a green LED was positioned by a calibrated translation stage with an increment of 0.5 mm. At each position corresponding charge division coordinate was calculated and plotted. Light level is approximately 100 photoelectrons.

C. *Intrinsic Spatial Resolution of the PMT*

In order to measure intrinsic resolution of the PMT we have used collimated parallel light beam produced by a green LED and a black shield with two holes of 0.3mm diameter. The shield was mounted directly on the PMT window so we were able to avoid light spreading in the window glass which thickness is about 1.5 mm. The LED intensity was adjusted to give about 0.1 photoelectrons per pulse. Only events corresponding to single photoelectron peak were recorded therefore converted photon should have coordinate of the first or the second hole of the collimator. The distribution and two-gaussian fit are shown on Fig.3. The reconstructed distance between two peaks well matches the hole separation of 1mm. The width of each of the two peaks is about 0.25mm RMS (or 0.6mm FWHM).

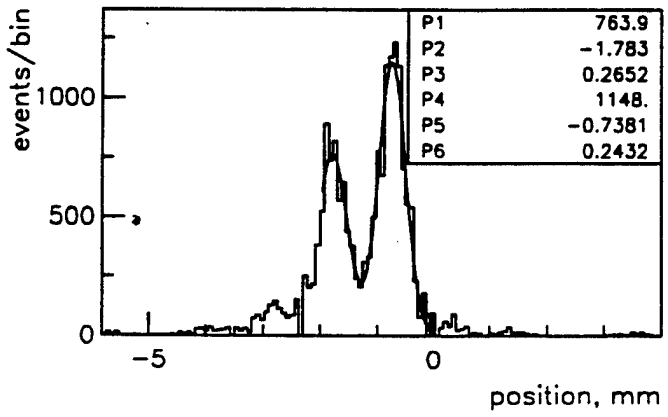

Figure 3: Reconstructed coordinate distribution for events selected around single-photoelectron peak +/- 1 RMS. Light source is a double beam produced by green LED through a collimator - black film with two holes of 0.3 mm diameter separated by 1 mm. Two peaks clearly separated at a distance of about 1mm.

D. *Single Fiber Response*

There are two difference between collimated beam and light coming from a fiber. First, fiber photons leave the surface of the fiber uniformly over the its cross-section. Second, these photons have an angular spreading of about 20-30 degrees, depending on type of the core and the cladding materials. These two factors together broaden the distribution of the photons converted on the photocathode. In order to evaluate this effect we have repeated previous measurement using instead of the collimated light beam - 0.5mm clear fiber coupled to a green LED and to the PMT by optical grease. The distribution is shown on Fig.4. It doesn't much differ from the distribution on Fig.3, which means that photoelctrons in this particular test are mostly distributed over two anodes or within 2 mm in physical space. Another useful test is how the resolution depends on number of registered photoelectrons. We found that the spatial resolution scales with the inverse of the square root of the number of the photoelectrons to well in excess of 20 photoelectrons. The results for different light levels are shown on Fig.5.

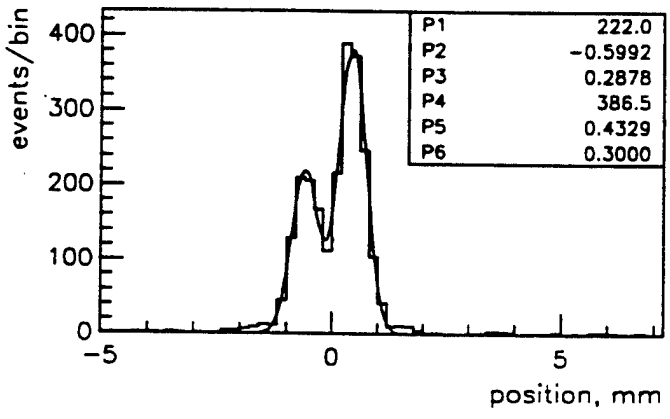

Figure 4: Reconstructed coordinate distribution for all events with amplitude greater than 0.5 photoelectron.. Light source is a green LED coupled to the PMT through a 0.5mm clear fiber giving an average of 0.1 photoelectron.

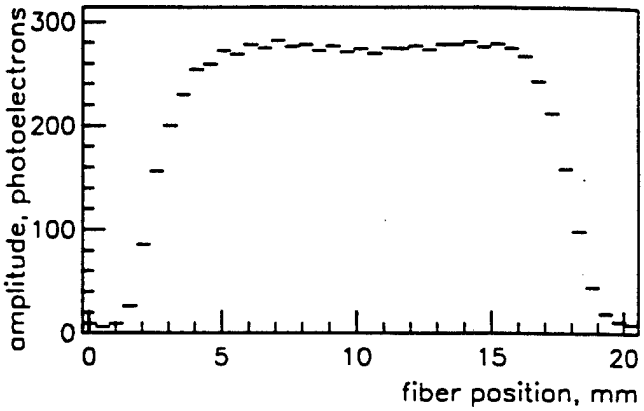

Figure 6: Visible light profile across the photocathode of the PMT. One end of a 0.5 mm fiber is coupled to a green LED, another end was moving in a proximity of the PMT face with a calibrated translation stage.

E. *Field of view test.*

All previous results were obtained in just few positions on the PMT window. Important questions also are how uniform and how big is field of view (photocathode area). Some edge effects are visible on Fig.2 so useful area for the first PMT tested was about 14*14mm. The result of a uniformity test is shown on Fig.6. The width of "uniform" area is about 15mm if one would agree to lose 50% of the signal. This lost would mean less number of photoelectrons registered and consequently some degradation in resolution on the edge.

As it was mentioned before, the last version of the PMT has wider active photocathode area. Therefore we have repeated the measurements reflected on Figs.2 and 6 and found that "useful" area of the last version of the PMT (based on the same criteria) is about 1mm wider in both directions (i.e. 16*16mm).

IV. Discussion

We are particularly interested in application of this PMT to the readout of wavelength-shifting fibers coupled to thin layers of scintillator crystals, for use in a PET detector were designing [6]. In this application, the spread of the light across a ribbon of photomultiplier has a FWHM about equal to the thickness of the crystal - 2 mm for our device. Achievable spatial resolution limited by this spread could be in principle a FWHM of 2 mm divided by the square root of the number of photoelectrons measured. This resolution is then further degraded by the spatial resolution of the fiber readout PMT, which from the above measurements is about twice better.

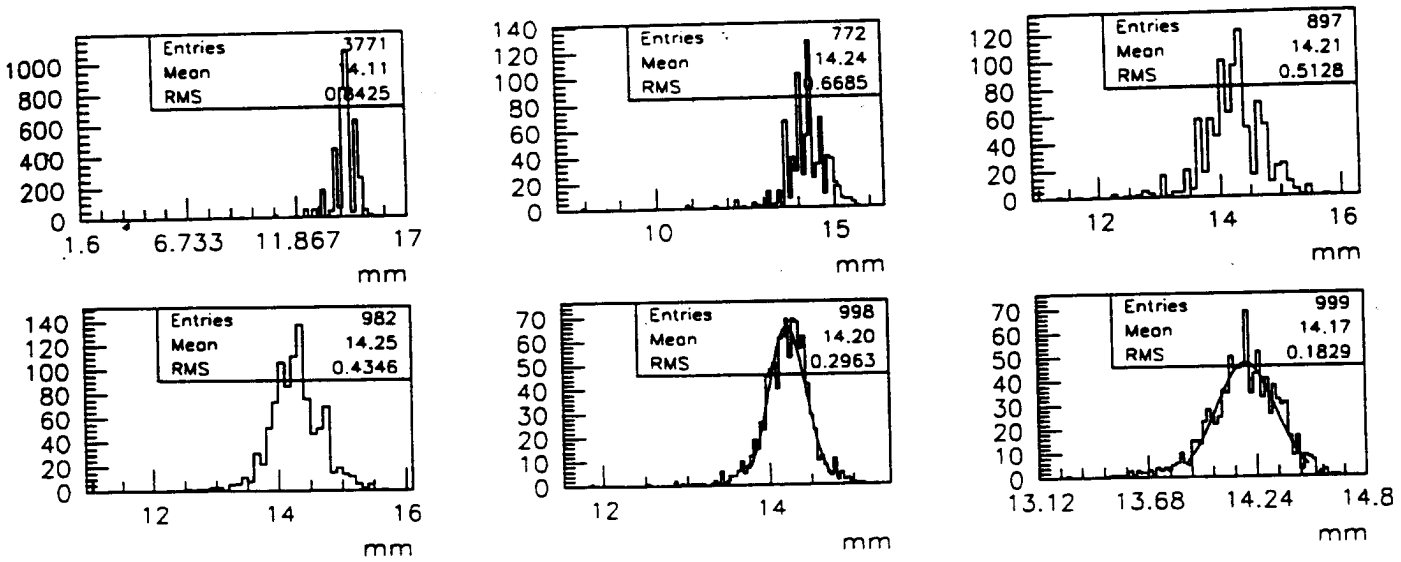

Figure 5: Reconstructed coordinate distribution for different light levels (upper row from left to the right: 1, 2 and 3 photoelectrons; bottom row from left to the right: 5, 10 and 20 photoelectrons). Light is coming from a green LED coupled to the PMT through a 0.5mm clear fiber.

Since the two effects are incoherent, we could preserve an ntrinsic resolution of our crystal-fiber readout design ındisturbed by the PMT itself. At a current cost of less than $1500 in single-unit quantities, this PMT is cost-effective in comparison with competing devices, particularly in multiplexed geometries such as one obtains when reading out one end each of many fibers at each PMT anode input (e.g. 14 ribbons of 1mm-diameter fibers each 14mm wide, for total of 196 fibers, may be read out with just two PMTs by differing the orientation of the readout PMTs by 90 degrees about the fiber axis at the two fiber ends - presuming that just 1 fiber of the 196 fibers on a given event). The level of multiplexing possible at low light levels is critically dependent on the spatial resolution achievable.

V. Conclusion

We have studied the properties of a photomultiplier with charge division readout suitable for scintillating or wavelength-shifting fiber applications with submillimeter resolution at low light levels of just few photoelectrons. It was shown that intrinsic resolution of the PMT is better than 1mm FWHM even for single photoelectron signals. The spreading of the light coming from the fibers to the PMT windows deteriorates resolution greater than electron optics does. From the other hand we have found that electrical cross-talks between anodes don't disturb achievable resolution and linearity of the charge division method.

VI. Acknowledgments

This authors wish to thank the staff of Hamamatsu Photonics K.K. for useful discussions and for their technical and production support.

VII. References

[1] Hamamatsu Photonics K. K., Electron Tube Center, 314-5 Shimokanzo, Toyoka village, Iwata-gun, Shizuoka-ken, 43801, Japan.

[2] M. Salomon et al., "Fiber scintillators coupled to a multianode photomultiplier as a high rate tracking detector", *IEEE trans. Nucl. Sci.*, vol. NS-34(1), pp.525-527, 1987.

[3] G. Comby et al., "Test of 64-channel PMT for imaging", *Nuclear Instruments and Methods*, vol. A269, pp.246-260, 1988.

[4] J. Bahr et al., "Test of a position-sensitive photomultiplier for fast scintillating fiber detector read-out," *Nuclear Instruments and Methods*, vol. A330, pp.103-114, 1993.

[5] S. Siegel et al., "Simple charge division readout for imaging scintillating arrays using a multi-channel PMT", *IEEE trans. Nucl. Sci.*, vol. 43(3), pp.1634-1641, 1996.

[6] W. Worstell et al., "Development of a high resolution PET detector using LSO and wavelength-shifting fibers", *1995 IEEE Nucl. Sci and Med. Imaging Conf. Record*, vol. 3, pp. 1756-1760, 1995

A 500k Event/Sec 12-Bit ADC System with High-Speed Buffered PCI Interface

V.G. Zavarzin[1] and W.A. Earle
Boston University, Department of Physics
590 Commonwealth Av., Boston, Massachusetts 02215
[1]currently at Tomotronics, Inc., Wayland MA 01778

Abstract

A low-cost replacement for popular LeCroy 2249 series charge-integrating ADCs with more than 100 times faster data throughput is designed and tested. The A/D converter chips used in the design provide 700 nsec conversion time and 25 MHz/32-bit parallel bus made of a twisted pair ribbon cable connected to a high-speed buffered PCI interface is capable of 100 MByte/sec data transfer to an ordinary IBM PC. The front-end of each ADC channel is equipped with an unipolar Baseline Restoration Circuit allowing use of AC coupling at very high signal rates (RF preamplifiers, HV decoupled signal sources like PMTs, wire chambers, etc.).

Being developed for Positron Emission Tomography, the system could also be used for a range of High Energy Physics applications, Spectroscopy, Medical Imaging and others where high event rate occurs.

I. Introduction

This paper presents the design and some performance results for the newly developed ADC sytem for use in our Positron Emission Tomography Project. The need for developing such a system arises from various limitations of commercially available A/D converters. For this particular project we wanted a portable system of about a hundred ADC channels with a moderate 10-bit resolution but capable of digitizing and transferring the data at up to 50k events per second rates. Systems satisfying our requirements exist but they employ very expensive and bulky standards like FASTBUS. Other less expensive solutions including LeCroy FERA[1] system are acceptable in terms of conversion rate and resolution but the speed of data transfer is too low for our application. Handling an event rate much higher than few kHz represents a serious technical challenge. For instance, in order to transfer 200 byte events at 50 kHz rate one needs a computer interface with at least 10 Mbytes/sec data throughput. Fortunately, recent progress in CMOS technology and Programmable Logic Devices (PLDs) allows one to design hardware meeting the above requirement at a reasonable cost. Also a range of A/D converter chips with 10-12-bit resolution and conversion time shorter than 1 usec is now available from different vendors for $8-15. In addition to this, In-System Reprogrammability of last-generation PLDs makes the debugging stage of the design cycle much shorter in time and less labor-intensive. All these reasons led us to developing our own ADCs with a PC-compatible interface.

II. System Architecture

A. General Description

We have chosen to implement the first version of the design in the CAMAC standard although we don't use the CAMAC backplane other than for the power supply. The idea was to be able to switch to a CAMAC-like crate containing just a moderate-wattage power supply in it, and get rid of the bulky, heavy and expensive full-featured CAMAC crate when the system has to be transported between hospitals for clinical trials. For the same reason it was convenient to have a trigger module residing in the crate right next to the ADC cards and have no extra NIM crate/modules.

In order to get the ADC data to the computer, we used a buffered PCI interface compatible with an ordinary PC, which we had previously developed for another project. More detailed descriptions of the trigger unit and the interface will follow in two separate paragraphs below.

B. ADC card

We decided to lay out 10 ADC channels with data interface per single CAMAC card although we had probably enough space to accommodate 16 channels. This choice was dictated by the number of I/O pins of the chosen PLDs. For our implementaton it's convenient to have delay lines embedded in the design, so the user doesn't have to externally delay analog signals. We used 200 nsec solid state delay lines from JBM[2] to equip each ADC channel.

The 12-bit data from all 10 channels are latched in parallel in two Altera [3] EPM7128S PLDs to be then transferred to the computer host. In order to achieve maximum possible data transfer rate to a computer and yet to keep the system reconfigurable we have chosen a unidirectional daisy-chain priority arbitration between ADC cards. It works as following: the first card has the highest priority, and as soon as it finishes its data transfer through the parallel 32-bit bus, the second card gains access to the bus and sends its data. Then the third card starts, and so on. The same PLDs mentioned above provide all control signals, daisy-chain arbitration and self-locking of the system (to prevent signal jamming during A/D conversion).

C. More Detailed Description of one ADC channel

One serious problem with a high signal rate is the so-called baseline shift, or floating of DC offsets when the signal rate fluctuates. This has to be eliminated before the signal integration so that the integral only represents pulse area. In order to design an integrator suitable for accurately integrating

small, fast PMT pulses which are superimposed on a DC offset voltage from decoupling capacitors, several issues are to be addressed. The first, is to have sufficient signal preamplification so that the integrating circuit can develop a reasonable output voltage for A/D conversion. Second, we have to compensate for the effect of changing DC offset on the integrated output, or, in other words, provide baseline restoration (BLR). And third, we have to use a sufficiently fast op-amp in the integrator that non-linear effects are not significant. Also the op-amp has to have very low input current in order to minimize drooping of the integrated signal.

Signal preamplification requires the use of very wideband amplifiers if signal fidelity is to be preserved. Although such amplifiers exist, they tend to exacerbate the DC offset problem because they usually have larger voltage offsets and input bias currents. A better approach is to use shaping amplifiers rather than linear ones, thereby allowing the use of lower bandwidth (and lower cost) amplifiers. If the shaping uses a single identical lag for each amplifier, then the input pulses will be stretched without adding overshoot. Lengthening the fast input pulses also allows us to use a slower op-amp for the integrator.

Baseline restoraton before the integrator input is relatively simple if, as in our case, the pulses to be integrated are unipolar. The circuit that removes the offset is usually called a baseline restorer and can be either passive or active. For the lowest offset, an active circuit is preferred. In our implementation, an OPA660 (Burr-Brown) transconductance amplifier senses the offset voltage to develop a feedback current that biases the preamplifier input in a way that the output offset is reduced to nearly zero. A diode is used in series with the output of the transconductance amplifier so that only one polarity of offset is corrected. The very high bandwidth of OPA660 (850 MHz) is required so that the baseline restoration acts only on the instantaneous offset rather than on the average. The final version of our BLR circuit shows a very small offset (less than 1% of the input amplitude) when an AC coupled pulser feeds the ADC input with a rectangular signals of 50 nsec width at a rate of 5 MHz (i.e. signal is present 25% of the time).

The op-amp used as the feedback integrator (we used LT1361 with JFET inputs from Linear Technology[3]) must have wide bandwidth so that its input summing junction remains at zero volts at all times as was mentioned above. If the bandwidth is insufficient, then the summing junction will move with the input signal and the integral will no longer be a linear function of the input pulse area. By using pulse shaping in the input amplifier, the required bandwidth of the integrator is reduced, allowing a wider choice in op-amps. Except during the integration interval, typically of order of hundreds nanoseconds, the integrator output is held at zero volts by two DMOS switches (SST215), one shorting the integrating capacitor and the other shorting the input to the integrator. These are extremely fast switches (one nanosecond on/off transition) which have to be are turned off to allow integration.

For the A/D converter itself we decided to use LTC1410 (also from Linear Technology, see [5]) - capable of 1.25M conversions per second with 12 bit resolution. We don't however use the power saving and microprocessor-type data output control features offered by the manufacturer.

D. Computer Interface

Technical details of the interface design lie definitely beyond the scope of this paper but a general description will be useful. The interface is a single PCI board residing in an IBM PC system block (currently the computer runs the Linux operating system but we are considering to write a driver for the interface under Windows 95/98 OS). It accepts 32 bits of data (TTL levels) in parallel, accompanied with a strobe signal, all of the above transmitted through a twisted pair ribbon cable of up to 10 m in length. Sequential data words have to have a minimum time separation of 20 nsec between them, providing a peak throughput of the interface itself of 200 Mbytes/sec. In our particular implementation we've chosen 40 nsec separation of sequential words within one event which saturates the data bus at 100 Mbytes/sec. Certainly such an enormous data flow can neither be recorded to a disk, nor be processed on the fly (at least with a single processor). Our target data flow was rather several Mbytes/sec and can be handled by a moderate IBM PC. In order to eliminate dead time when the CPU reads the data out, the PCI interface has two memory banks: when the first is full and is being read by the computer, the second bank is available for writing into it from the ADCs.

In the case of our initial implementation of 5 10-channel cards, the whole data transfer lasts:

$$5 \times 10 \times \tfrac{1}{2} \times 40 \text{ nsec} = 1 \text{ microsec},$$

(½ is here because data words get transfered by pairs). Combined with the conversion time of 700 nsec and small daisy-chain overhead it yields a maximum throughput of about 500k events per second if the computer is powerful enough. For a greater number of ADC cards the maximum throughput will be decreased linearly.

E. Trigger Board/Gate Generator

Strictly speaking, the above ADC cards require only one external signal - TTL-leveled "Gate" determining how long input analog signals are to be integrated. The end of "Gate" signal starts A/D conversion in all ADC cards simultaneously.

We found it convenient to combine discriminators, coincidence circuit and gate generator (with apropriate gate delay and width adjustments) in one CAMAC card, together with TTL pulser for calibration needs. All logic of the above functions fits within just one inexpensive Altera PLD chip - EPM7064SQC44. Currently we have four independent discriminator channels (based on LeCroy discriminator chips - MVL107S [1], with ouputs converted from ECL to TTL). They work reliably with a minimum threshold of about 20 mV. The width and the delay of the "Gate" signal are easily programmable in order to satisfy any particular requirements.

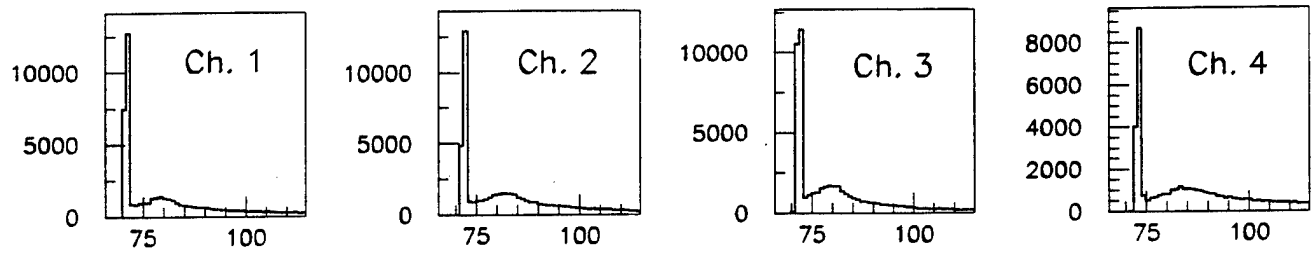

Figure 1. Example of amplitude distributions for four randomly chosen channels. The pedestal spike widths are about 1.3 LSBs FWHM. Acquired with R5900 PMTs and 10x preamplifiers attached to the above ADCs. Average signal is very small (~0.8 photoelectrons) so single-photoelectron peaks are clearly visible.

Again, because of the In-System Reprogrammability feature of these Altera PLDs, it's easy to reconfigure the logic of the trigger, say, for instance from total OR of all input signals to some more complicated coincidence of their pairs, etc.

III. Performance Tests and Results

The very first check we have undertaken after initial debugging of the design was to see if the data gets corrupted during transfer from ADCs to the computer. Fourtunately we didn't find any damaged datawords among many millions of recorded bytes. It proves that the daisy chain and twisted pair databus are functioning properly.

A second important test is determining the maximum speed of the system. We found that a single processor Pentium-II/266 MHz PC is capable of recording of about 35k events (100-byte size) per second to its hard disk. This is a pure disk limitation, since the speed of just reading the data into PC memory exceeded 100k events per second.

We measured the widths of pedestal distributions in presence of high voltage on PMTs with 10x preamplifiers connected to several ADC channels (see Fig.1). The average width was about 1.3 LSBs FWHM.

We didn't spend a lot of time characterizing overall non-linearities, but we did check the differential non-linearity in several channels by acquiring very high statistics of smooth amplitude distribution. In good agreement with the manufacturer's specification [5], non-smoothness of measured distributions did not exceed 30%.

Also we measured long and short-term drifts of the ADCs and found that the pedestals in all channels shifted by 1-2 LSBs (Least Significant Bits) within 1 minute after turning on the power supply. After this first minute, the values in most of the channels stayed stable vs time and temperature (we have repeated the measurements for several weeks) within +/-1 LSB.

Among other parameters characterizing ADC perfomance are:

integration gate width - 20 nsec -- 20 usec;
sensitivity - 0.2 pC/LSB;
input impedance - 50 Ohm.

Power requirements per ADC board:
+6V - 0.5A, -6V - 0.4A, +/- 12V - 0.12A, or about 8.5W of total power consumption. As one can see, the heat dissipation is not substantial so it doesn't need forced airflow for the cooling.

IV. Acknowledgments

We are grateful to Eric Hazen and Bill Worstell of Boston University for their constant interest in this work and for discussions they participated in. We would like to thank Andrey Chertovskih and Alexei Nikiforov of Budker Institute of Nuclear Physics (Novosibirsk) for their work on the PCI interface. We would also like to thank Yury Yudin, and Pavel Stepanov of the same Institute for their participation in the project.

V. References

1. LeCroy 1997 Research Instrument Products, LeCroy Corporation, Chestnut Ridge, NY 10977, USA.
2. JBM Electronics, Inc., Bedford, NH 03110, USA.
3. Altera Corporation, San Jose, CA 95134, USA.
4. Linear Technology Inc., Milpitas, CA 95035, USA.
5. "LTC1410 12-bit, 1.25MSPS Sampling A/D Converter with Shutdown ", datasheet from Linear Technology Inc.

DEVELOPMENT OF A HIGH-RESOLUTION PET DETECTOR USING LSO AND WAVELENGTH-SHIFTING FIBERS

William Worstell, Olof Johnson, and Valery Zawarzin
Boston University Physics Department
590 Commonwealth Avenue, Boston, MA 02215

Abstract

By using wavelength-shifting fibers coupled to thin plates of LSO and to photomultipliers, we have demonstrated spatial resolution of 2mm FWHM for photocapture events. Optimized systems are believed to be capable of better than 1mm FWHM resolution, without requiring either very small crystals or large numbers of photosensors. With this sensor resolution, annihilation acollinearity dominates system resolution for large PET rings. By radially stacking alternating layers of thin crystals and wavelength-shifting fibers, a direct depth-of-interaction measurement is possible. Energy measurements and coincidence timing may be provided by trigger photomultipliers in a dual-photodetector geometry. Results from computer simulations and component response measurements on proof-of-concept prototypes are presented.

I. INTRODUCTION

We are developing very high-precision PET detector modules with depth-of-interaction sensitivity, using a new design incorporating wavelength-shifting fiber readout of thin LSO crystals. By building modules from thin crystal layers stacked radially, one can obtain both depth-of-interaction information and fine spatial resolution in the tangential and axial directions. Component-level testing of this technique has demonstrated <2 mm FWHM spatial resolution for 2mm thick LSO crystals. Optimization and extrapolation to full PET systems may yield devices with resolution as small as 1mm FWHM using 1-2mm thick crystal layers; the resolution is expected to vary linearly with the crystal layer thickness. Depth-of-interaction sensitivity is essential for uniformly high-precision PET throughout a large field-of-view, if one is to preserve the detector thickness needed for high efficiency and high event statistics. Depth-of-interaction sensitivity also minimizes the necessary detector diameter, thereby decreasing both acollinearity errors and system costs, while increasing solid angle coverage. Our modular device design permits testing of a variety of detection geometries, including geometries appropriate for laboratory animal, human brain, and dedicated PET mammography applications.

II. MATERIALS AND METHODS

We have used ribbons of wavelength-shifting fibers to determine the positions of gamma-ray interactions within thin LSO scintillator crystals. Within a wvaelength-shifting fiber, fluorescent dopant molecules absorb short-wavelength incident photons and then isotropically emit secondary longer-wavelength photons. One can use the fluorescent re-emission process effectively to inject light into a light pipe through the sides of the pipe, since a fraction of the re-emitted light is trapped and piped along the fiber. In this way, the fiber becomes a light sensor, with short-wavelength light as input and long-wavelength light as output. An array of parallel fibers (i.e. a fiber ribbon) may then be used to measure incident light profiles in one dimension; two perpendicular ribbons (on opposite faces of the thinscintillator crystal) can provide a two-dimensional incident light profile measurement. Gamma-ray interactions in dense scintillators result in a very nearly point-like light source, because of the short range of secondary photocapture electrons. For polished high-index scintillator crystals, only light emerging nearly normal to the crystal surface escapes total internal reflection, resulting in an emission spot with diameter comparable to the crystal thickness. We earlier described this technique as applied to BGO crystals read out with red wavelength-shifting fibers [1].

In the present work we have focussed on the fast, high-Z, high-brightness scintillator Lutetium Oxyorthosilicate or LSO [2]. We have performed most of our initial measurements on two samples of LSO, each 2mm x 10mm x 10mm, which we obtained from Schlumberger-Doll Research [3]. These crystals were hand-polished on their large surfaces, and all surfaces not coupled to fibers were painted black. Fibers were coupled to crystals with a high-index epoxy (n=1.65), EpoTek OG127 [4]. For readout fibers we used 1-mm diameter, round, doubly-clad wavelength-shifting fibers from Kuraray Corp [5]; we obtained our best spectral matching with their spectral type Y-11. Doubly-clad fibers have a core refractive index of 1.60, an inner cladding index of 1.49, and an outer cladding index of 1.42; this yields a numerical aperture of 0.74 and a trapping efficiency of about 7% per fiber end for the re-emitted light (the remaining 86% of the re-emitted light is not trapped and emerges through the sides of the fiber ribbon).

Our initial tests have been carried out with the apparatus illustrated schematically in Figure 1. We form a pencil beam of 511-keV gamma rays by requiring the coincident detection of two back-to-back annihilation gammas produced by a nearly point-like Na-22 positron source. The first of the two gammas strikes a small 1mm x 3mm x 15mm LSO "triggering" crystal through its 1mm x 3mm entry face, while the partner ray goes through a 1mm lead collimator to the "target" 2mm x 10mm x 10mm crystal. The "target" crystal is coupled to a ribbon of 10 parallel 1mm diameter round wavelength-shifting fibers and to a trigger PMT. Since the light collected by the trigger PMT is proportional to the energy deposited in the target crystal, we are able to select events with photocapture of a pencil-beam gamma by the target crystal, by requiring a large trigger signal in coincidence with a signal from the "triggering" crystal. The "triggering"

0-7803-3180-X/96$5.00©1996

LSO crystal and its PMT, the Na22 source and collimator are all mounted on a calibrated X-Y adjustable table, while the "target" crystal and PMT with fiber assembly are fixed; in this way, a pencil beam can be precisely directed into the "target" setup, and may be swept along the target. All measurements are made with unshaped signals directly coupled to charge-sensitive ADCs (LeCroy 2249W); the timing gate width was 150nsec and only photopeak events were used for analysis.

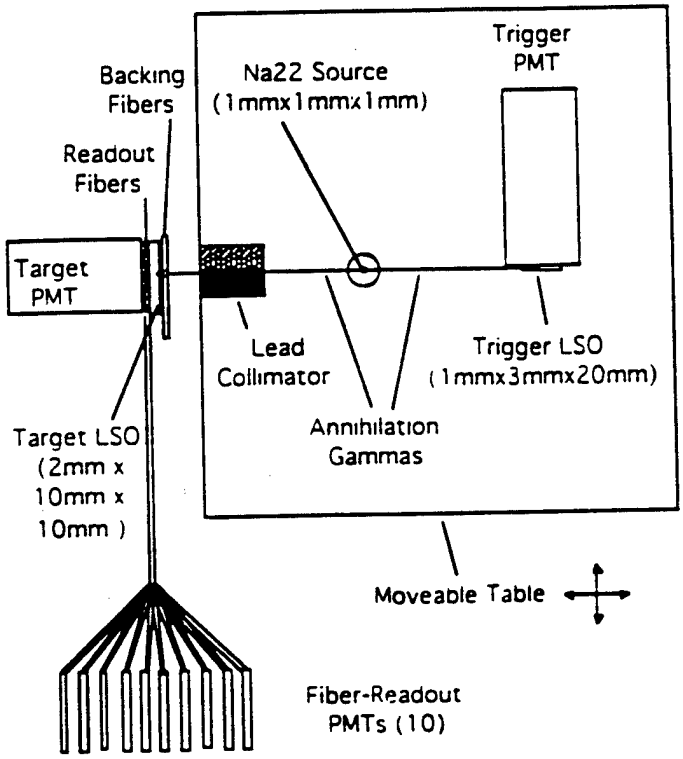

Figure 1 Schematic illustration of test apparatus.

Each of 10 fibers coupled to the target crystal is read out by an individual Hamamatsu R1635 PMT, allowing us to record the light profile and centroid position within the fiber ribbon on an event-by-event basis; all PMTs were calibrated and outputs converted to photoelectrons. The index of refraction of LSO is about 1.8, so we used the high-index optical epoxy for coupling crystals to fibers. The thin sides were blackened with an opaque mixture of high-index epoxy and xerographic toner (to simulate a larger crystal). Fibers were coupled to both of the large LSO surfaces, with 30cm long fibers having one polished end at the readout PMTs and their other ends 1 cm from the crystal. Light trapped at the optical interface between cladding and air ("cladding light") was removed by an opaque fiber holder gripping each fiber before its coupling to its readout PMT. The fiber/PMT optical interface was made with optical grease.

We have developed a complete Monte Carlo simulation of our detector's optics, including all optical interfaces and the correct geometry for round multiclad fibers. We have also developed a detailed radiation transport Monte Carlo simulation to study the effects of gamma-ray scattering and attenuation both in objects being imaged and within the detector itself. The latter simulation is based on the GEANT detector simulation code commonly used in high-energy physics, which allows for simple implementation and modifications of the detector geometry through a flexible and powerful user interface. We generate gamma-rays from our source phantom according to a positron range distribution appropriate to ^{18}F, and with acollinearity between the annihilation gammas sampled from a Gaussian distribution with width 0.3 degrees. The detector resolution was usually taken to match the (not-yet-optimized) response functions measured with our test apparatus, and matches the measured dependence on light yield (gamma ray energy).

We have also begun work on making images with simulated data using a simple 2-D filtered back-projection reconstruction algorithm, for a number of test phantoms. In particular, we have looked at the benefits of depth-of-interaction resolution for small-diameter systems such as for use with laboratory animals. For some of these studies we have simulated a 1/2-scale version of a standard resolution phantom, with resulting 10cm diameter axially symmetric phantom viewed by a simulated 20cm diameter detector ring. To contrast with our detector, we have modelled a device without depth-of-interaction sensitivity, consisting of 8mm thick LSO on a 20cm diameter ring. For the radially-segmented fiber readout 20cm diameter ring we have used a total crystal thickness of 24mm, which would result in improve coincident efficiency by a factor of 3.2 relative to a 8mm thickness ring.

A wide range of system design options are open with a radially-segmented fiber readout geometry, and we have begun our exploration of these options with a baseline module having thickness 24mm and area 128mm x 128mm. Our plan is to construct and test at least one such module within the coming year. Assuming 2mm thick LSO layers and 1mm diameter fibers, this requires the readout of 13 x 128 = 1664 fibers per module. Multiplexing is clearly necessary in order minimize the cost for readout photomultipliers and digitizing electronics. One method for such multiplexing, employing separate readout of two fiber ends, is illustrated schematically in Figure 2 below. Other schemes, including mirrored fibers and two different colors of waveshifting fiber, are possible.

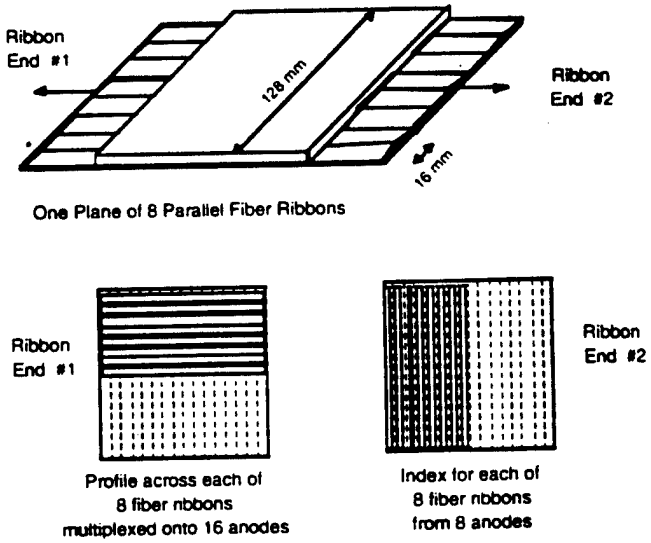

Figure 2: Multiplexed readout of fiber Ribbons using 16-channel multianode photomultipliers.

We have been testing a new R5800-L16 multianode photomultiplier from Hamamatsu Corporation, which combines 16 input pixels each 1mm x 16mm in area with a very narrow pulses (2ns FWHM) and good single-photoelectron resolution [6]. By reading out the two ends of multiclad fiber ribbons to two different multianode PMTs, one can read out as many as 256 fiber ends per PMT. Multiplexed readout of fiber ribbons corresponding to different crystal layers is also possible and probably desirable. If 0.5mm-diameter fibers are used, the physical limit is 1000 fiber ends per PMT. Although not indicated in the figure, it may be desirable to break up each 128mm x 128mm crystal plane into 64 16mm x 16mm optically isolated "cells" to reduce multiplexing cross-talk.

Electronics channel count can be minimized by charge-division readout (two signals rather than 16 from each photomultiplier) as is typically done with crossed-wire position sensitive PMTs. We have measured 20ns pulse widths (into a 50 ohm load) and <<1mm resolution at 20 photoelectrons for charge division readout of our R5800-L16 PMT, using 100 ohm resistors to connect the anodes. In principle, the readout of a 16-layer module with area 128 mm x 128mm using 0.5mm fibers could require just 4 multianode photomultipliers (at a current cost of $1500 each), with 8 associated fast ADC channels.

III. PRELIMINARY RESULTS

Our measured light yield for fiber readout of LSO crystals is in general agreement with our expectations. The light output for LSO is quoted at various levels in the literature, and is a strong function of the concentration of Cerium dopant: the most recent work cites a light yield of 20,000 photons/MeV deposited or about 10,000 photons per annihilation gamma photocapture event for LSO with a Cerium concentration of 0.22% [7]. Monte Carlo simulations predict that more than 25% of emitted photons should emerge from a given crystal readout face into the corresponding fiber ribbon, with photons incident at large angles (relative to the surface normal) totally internally reflected. Direct coupling of a photomultiplier with 20% quantum efficiency (when averaged over the LSO spectrum) to LSO with this brightness should thus give about 500 photoelectrons: this is consistent with our measured light yield in this "direct coupled" geometry. The next link in the optical chain is the match of the emission spectrum of the LSO crystal to the absorption spectrum of the fiber. This factor is about 60%, based on convolution of published LSO emission spectra and Kuraray's absorption spectra for Y-11. We thus expect that roughly 1500 scintillation photons are absorbed and re-emitted within the wavelength shifting fibers in each photocapture event.

Multiclad fibers trap 14% of their re-emitted light, or 7% per fiber end. Our measurements comparing light yield with multiclad vs. singly clad fibers, where the latter have 4% trapping per end, confirms this trapping fraction for the multiclad fibers we used. This implies that with multiclad fibers about 100 photons are piped toward each fiber end each photocapture event. Finally, some photons were attenuated within the readout fibers (such self-absorption filters out the shortest-wavelength photons, and typically results in re-emission of an unpiped green photon), and a few photons arriving at the photomultiplier were reflected at the optical interface between fiber and photomultiplier. Our estimates of these effects were that we had about 80 photons entering our fiber readout photomultipliers each photocapture event, where they had an average quantum efficiency of about 10% for being converted to photoelectrons (Y-11 has its emission peak at 495 nm). This accounts for the roughly 8 photoelectrons which we observed per photocapture event with our test apparatus. This light yield, although small, is sufficient for multiplexed readout with good efficiency. Additional light yield may be achievable by using fibers with a better spectral match to LSO emission, by using PMTs with better quantum efficiency for green light (green-extended R5800-L16 PMTs are currently under development at Hamamatsu) or by obtaining brighter LSO.

The emission light profile from LSO crystals and the measured spatial resolution achieved at our current light level is shown in Figure 3 below. The resolution horizontal scale has been calibrated by moving the pencil beam in our test fixture across the crystal by known increments and measuring the resulting changes in the measured centroid position.

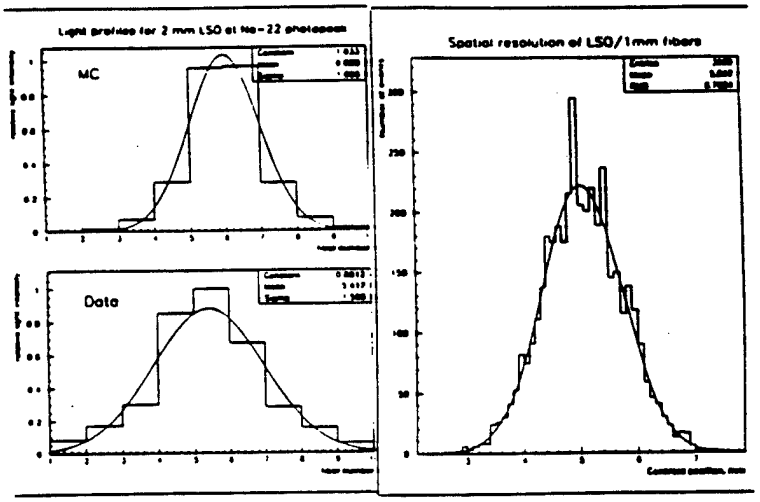

Figure 3: Measured response of LSO/Fiber test apparatus.
Left = Predicted and measured profile of light collection.
Right= Measured spatial resolution using centroids.

By measuring the distribution of photoelectrons across the fiber ribbon for photocapture events, we were able to reconstruct the event position with an accuracy of about 0.7mm RMS. There is still a contribution from the beam width to this resolution, for which we have not corrected. The accuracy of our coordinate measurement varies directly with the width of the light emission profile, so that the quality of crystal surface finish is important. Our Monte Carlo optical simulation predicted a profile of about 1.0mm RMS for a 2mm thick ideally polished LSO crystal, while the measured profile had a width of 1.6mm RMS. Evidently, our crystal surface preparation and fiber coupling could be improved. Spatial resolution improves with light yield like the square root of the number of photoelectrons N, and ideally the resolution should approach the profile width / $\sqrt{N}$.

We have carried out a simulation for a geometry appropriate to Positron-Emission Mammography, which we have simplified as two parallel planes separated by 10cm of water. Figure 4 illustrates the line-spread function (LSF) predicted for a perfect detector (due to just positron range and acollinearity), for fiber readout from 1mm thick LSO, and for fiber readout from 2mm thick LSO; the latter two are extrapolated from our non-optimized test results. It is apparent that range and acollinearity effects are very small.

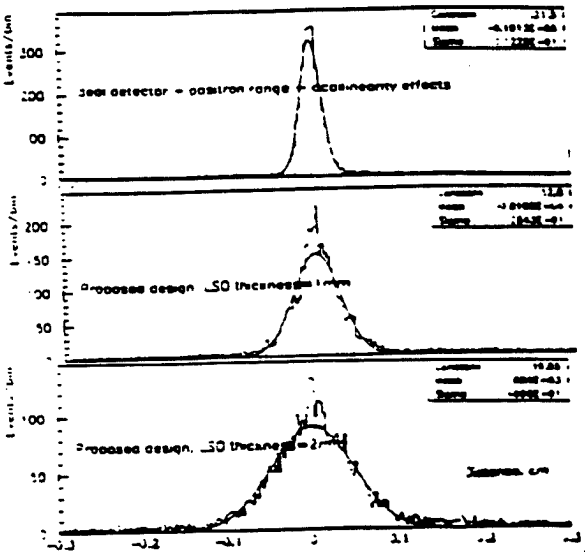

Figure 4: Simulated line-spread function and intrinsic limits.

As mentioned earlier, we have contrasted the simulated response of our proposed detector with that of a device with comparable spatial resolution but without depth-of-interaction sensitivity; both were formed into 20cm diameter rings.

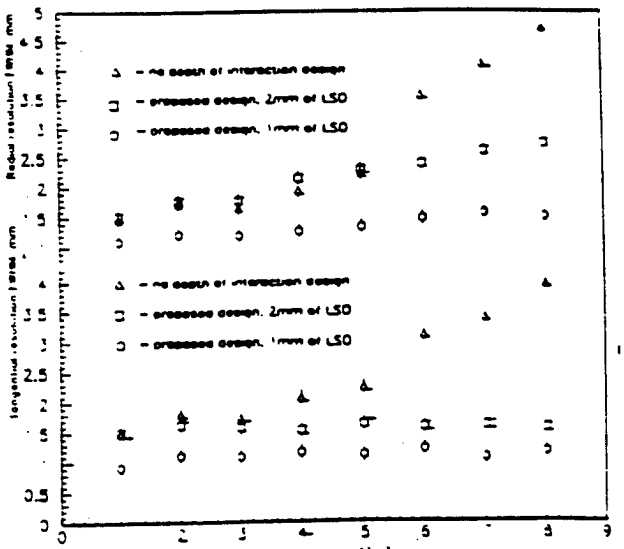

Figure 5: Resolution vs. radial position.
TOP = No DOI. MID = 2mm/ fiber. BOT= 1mm/ fiber

Figure 5 shows the reconstructed resolution as a function of distance from the center of the field-of-view for each device). Again, we have used the measured but not-yet-optimized resolution from our test apparatus as input to this simulation; in addition, we have indicated the resolution which should be achievable with 1mm thick LSO layers with our fiber readout. While our device has very nearly uniform resolution over the entire field of view, the device without depth-of-interaction sensitivity has clear resolution degradation away from the center of the field of view.

IV. DISCUSSION

Radially segmented readout of thin LSO crystals with wavelength-shifting fibers has the following advantages:

- Very High Spatial Resolution
- Depth-of-Interaction Measurement
- High Rate Capability
- Potential for Low Cost
- Flexible Readout Options

Unlike most designs for very high-resolution PET detectors, this design scales readily to large systems while preserving high efficiency and fine resolution; it also only makes use of existing photosensor and electronics technology.

Since the spatial resolution scales linearly with the crystal thickness, extremely fine spatial resolution should be achievable with small-diameter rings. Resolution blurring due to acollinearity (about 2.2mm FWHM per meter of ring diameter) can be made to dominate system resolution for large rings; smaller rings can achieve submillimeter resolution with high efficiency across a large field of view (if short-range positrons like 18F are used) by using very thin crystal layers. Axial resolution is naturally comparable to tangential resolution, and to depth-of-interaction resolution. Double-hits from Compton-scatters within the detector (which can degrade resolution of block detectors) are readily identifiable with suitable electronics, since they will almost always deposit energy in more than one crystal layer. Use may be made of Compton scattered (rather than photocaptured) events in small rings imaging objects with little scatter, with only a small degradation in spatial resolution. Finally, detector modules may be combined in a "gapless" geometry by radially overlapping in a pinwheel arrangement as shown in Figure 5; any oversampling which which results in the overlap regions may be corrected using depth-of-interaction information.

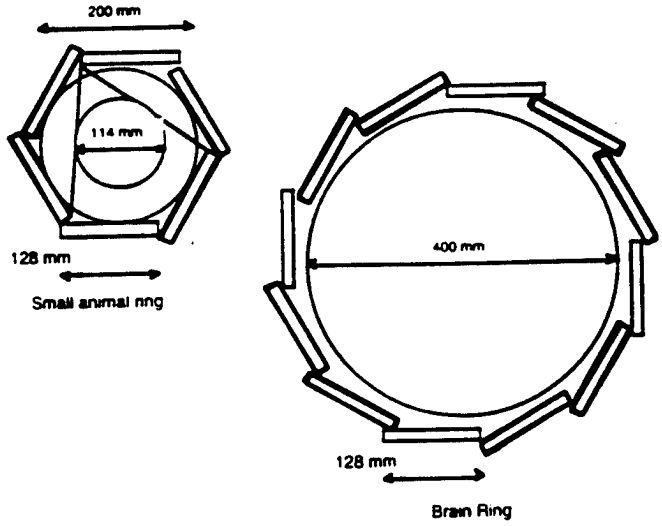

Figure 5: Conceptual System Geometries with Fiber Readout

Depth-of-interaction measurement is critical for preserving very fine spatial resolution throughout a large field of view, without compromising on detector coincidence efficiency (which is critical for the statistics needed to made a high-resolution image). Depth-of-interaction sensitivity permits a reduction in ring diameter, which pays several dividends: lower system costs for less scintillator and fewer readout channels, smaller effects from acollinearity, and higher efficiency through greater solid angle coverage. The last comes at the price of increased scatter acceptance, but this trade-off is already being chosen in the selection of 3-D over 2-D PET. Increasing the module size (both in axial and tangential dimension) yields a more cost-effective readout by using longer readout fibers, which increases the detector volume/PMT area ratio; the price paid is lower rate capability.

With fully multiplexed readout (including in depth) of 128mm x 128mm area modules, a rate capability of >1Mhz/module should be achievable. The 45ns decay time of LSO permits signal integration over 150ns, with digization of charge-division signals to the required 7-bit resolution possible in less than 1 microsecond. Time correspondence of 8 PE signals from 45ns scintillator has high efficiency within a 10-20ns window. The coincidence timing (for singles rejection) and energy resolution achievable with an all-fiber readout are more problematic. If necessary, fiber readout can be supplemented with large trigger PMTs which would collect the re-emitted but non-trapped light which emerges through the sides of the wavelength-shifting fibers and to which both fibers and crystals are transparent. Our measurements have shown that although less than 10% of LSO light passing through one fiber layer is absorbed in the next, the layers which are opaque to LSO light are very transparent to fiber light. Supplemental readout with large trigger PMTs would yield hundreds of photoelectrons, sufficient for 1ns coincidences and energy resolution limited by effects other than photostatistics. Large-area photodiodes might be substituted for photomultipliers to preserve compatability with operation in a magnetic field, if necessary.

Fiber readout of LSO is potentially quite cost-effective, presuming that the bulk price of LSO continues to fall. It is currently at $50/cc in quantities of 100's of cc's, and is projected by the crystal grower to fall to $15/cc in about 1 year. At this price it becomes competitive with BGO, and fiber cutting and polishing costs become significant (especially for very high-resolution devices with small crystals). The crystal cutting and polishing required for the thin flat crystals used with fiber readout is significantly less than for the long thin crystals in other detectors, and we will carefully check how our performance varies with crystal surface treatment. The cost for 4 multianode PMTs to read out fibers from a 128mm x 128mm module is comparable to the 25 1" PMTs which would be required to read out the same area in a block detector; if larger modules have sufficient rate capability, fiber readout costs fall still further. The cost of fibers in quantity, about $1/m for 0.5mm diameter, makes the fiber cost small in comparison to crystals and PMTs. Finally, the electronics channel count reduction yields savings, reducing the 25 ADCs for the above block detector to 8 in our design.

Although our initial results have been encouraging, we have been somewhat handicapped by the availability of only small samples of LSO. This situation has now changed, and we anticipate the availability of hundreds of cc's of LSO by early 1996. Our plan is to further optimize and to construct large modules with this new material as soon as possible.

V. CONCLUSIONS

We have demonstrated that wavelength-shifting fibers can be used to read out gamma-ray interaction positions within thin sheets of LSO crystals, with high efficiency. The spatial resolution achievable (FWHM) is less than the thickness of the crystal layer being read out. Consequently, by constructing a detector from a thick stack of many thin layers, one can combine very fine spatial resolution with depth of interaction sensitivity and high efficiency. With optical multiplexing at the crystal layers and at the readout photomultipliers, a cost-effective design with extremely high spatial resolution is achievable; this design is readily scaled to large-diameter systems. During the coming year, we plan to constract one or more 128mm x 128mm x 20mm thick modules to test and optimize this design.

ACKNOWLEDGMENTS

We would like to thank Dr. Charles Melcher of Schlumberger-Doll Research, for providing us with LSO samples, and to thank Kuraray Corporation for providing us with samples of their Y-11 multiclad wavelength shifting fiber. We are grateful to Hamamatsu Corporation for the loan of a R5800-L16 multianode PMT which was used in this work. We would also like to thank Charles Burnham of Massachusetts General Hospital for many helpful discussions regarding PET systems. This work was supported through the Boston University Center for Photonics Research, under Grant No. N00014-93-1-1186 from the Office of Naval Research.

REFERENCES

1 W. Worstell, S. Doulas, O. Johnson, C. Lin, "Scintillator Crystal Readout with Wavelength-Shifting Optical Fibers," IEEE Medical Imaging Conference Proceedings, 1994.

2 C.L.Melcher and J.S.Schweitzer: "Cerium-doped lutetium orthosilicate: A fast, efficient new scintillator", IEEE Trans. Nucl. Sci. NS-39, pp. 502-504, 1992

3 Schlumberger-Doll Research, CT

4 Epotek Corp., Billerica, MA

5 Kuraray Corp., 200 Park Ave., New York, NY 1016

6 Hamamatsu Photonics, 360 Foothill Road, Bridgewater, NJ 08807

7 T. Ludziejewski et. al. "Advantages and Limitations of LSO Scintillator in Nuclear Physics Experiments", IEEE Trans. Nucl. Sci 42 Pg 328-336

First Results with High-Resolution PET Detector Modules using Wavelength-Shifting Fibers

W. Worstell, *Member, IEEE*, O. Johnson, H. Kudrolli, and V. Zavarzin
Boston University Physics Department and Center for Photonics
590 Commonwealth Avenue, Boston, MA 02215

***Abstract*-- We have constructed and tested prototype PET detector modules incorporating wavelength-shifting fiber ribbons alternating with thin CsI(Na) scintillator plates in multilayer stacks. Modules with cross-sectional area of 11cm x 11cm and with 9mm of total crystal thickness have been tested. A reconstructed spatial resolution of 3 mm FWHM has been obtained for a line source, with an energy resolution of <20% and a time resolution of 25ns FWHM. Energy measurements and coincidence timing are provided by 4 photomultipliers in an Anger array on one 11cm x 11cm module face. Multiplexed fiber readout has been implemented with multianode photomultipliers coupled to several fiber ribbons. The methods and resolution achieved are readily extended to larger systems in a straightforward and cost-effective manner. Results of tests with several phantoms are presented.**

I. Introduction

Perpendicular ribbons of wavelength-shifting fibers may be used to determine the position of gamma-ray interactions within thin scintillator crystals, with the obtainable spatial resolution comparable to the crystal thickness [1-2]. By building a multilayer stack of alternating thin, flat crystal layers and perpendicular fiber ribbons, we have measured gamma-ray interaction energies and positions in 3 dimensions with good accuracy and efficiency. We have constructed and characterized such a device, and have imaged 3 test phantoms.

Depth-of-interaction sensitivity is needed to preserve the spatial resolution of PET detectors when accepting events whose lines-of-response intersect detector elements at significantly oblique angles. The parallax which leads to errors without depth-of-interaction sensitivity may, however, be used to provide information on object depth-of-field in a limited angle geometry, for a device with depth-of-interaction measurement capability. This is particularly significant in the design of devices for Positron Emission Mammography (PEM) where two parallel plate detector elements above and below a breast may be used to detect coincident gammas [3-4].

For a device whose field of view is comparable to the detector separation, events with significant parallax may be acquired and used to resolve features at different depths-of-field between the two plates. Other groups have used back-projection imaging in this geometry, while we have used 3-D limited-angle tomographic reconstruction incorporating an iterative reconstruction algorithm based on Inverse Monte Carlo methods and Image Space Reconstruction.

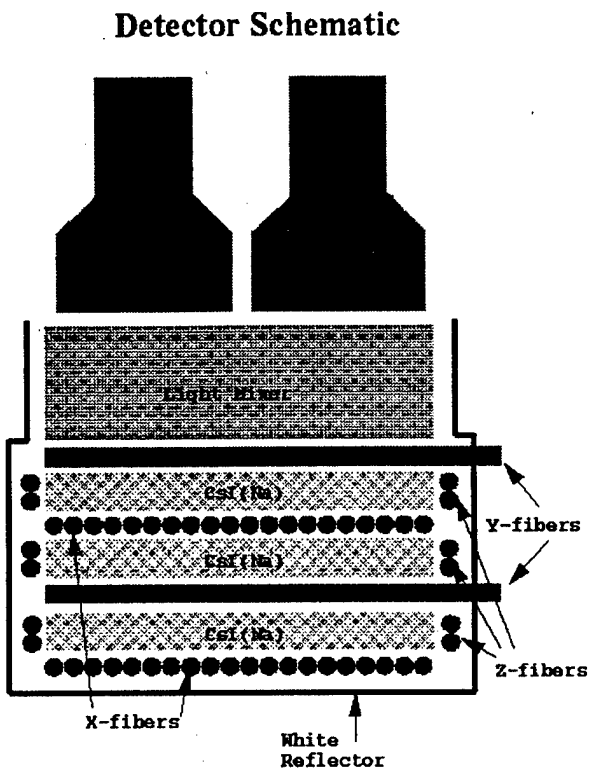

Figure 1: Schematic Illustration of detector geometry. Three thin layers of CsI(Na) scintillator alternate with perpendicular fiber ribbons. Edge fibers are used to measure depth-of-interaction, while Anger PMTs view the laminated fiber/crystal block through a light mixer; the block walls are lined with white reflector.

A schematic illustration of our device geometry is given in Figure 1. For flat polished crystals, total internal reflection guides scintillation light emitted at shallow angles with respect to the crystal surface toward the crystal edges, while light emitted nearly normal to the surface exits the crystal above and below the gamma ray interaction point. This exiting light position may be sensed locally by wavelength-shifting (fluorescent) optical fibers, which absorb the primary scintillation photons and isotropically re-emit secondary photons at longer wavelengths.

Perpendicular fiber ribbons (X-fibers and Y-fibers) on opposite sides of a thin, polished crystal layer may thus be used to measure gamma-ray interaction positions in two dimensions; further fibers at the edges of crystal layers (Z-fibers) may be used to sense scintillation light which was totally internally reflected within a layer, providing information on depth-of-interaction within a multilayer stack. Alternatively, one may read out fiber ribbons from different

depths within a multilayer stack with different photosensors, but this is costlier than the edge-fiber decoding method.

Coupling scintillator crystals to wavelength-shifting fibers is much cheaper than direct fiber coupling with transparent fibers, because of the smaller photoconverter (e.g. multianode photomultiplier) area required to read out fibers from a given area of scintillator. With wavelength-shifting fiber readout, the fiber readout area increases in proportion to the scintillator perimeter, while for transparent fiber readout the fiber readout area increases in proportion to the scintillator area. Within a wavelength-shifting fiber, a small fraction of the secondary photons emitted at angles near that of the fiber axis are piped to fiber readout photosensors, while most emerge transversely from the fibers and traverse both scintillator and fibers within a multilayer stack transparently. This unpiped light can be collected with a standard Anger array on the module surface to provide energy and trigger information as well as approximate interaction coordinates. These approximate coordinates can then be used to de-multiplex the readout of several fiber ribbons which may then be read out with the same position-sensitive multianode photomultiplier. Multiplexed fiber readout is important for limiting both system component costs and electronics channel counts.

The above method decouples the event energy, timing, and triggering functions, which are performed by the Anger system, from the precise event position determination in 3 dimensions, which is performed by the fiber readout system. This is important since the light yield from the wavelength-shifting fibers, although easily sufficient for precise coordinate determination and high efficiency, is insufficient for precise event energy and timing determination.

The performance achievable with wavelength-shifting fiber readout of scintillator crystals depends critically upon the choice of scintillator material, the quality of crystal surface treatment and related optical coupling parameters, and finally upon the device geometry and in particular the crystal layer thickness. In the results presented below we have used CsI(Na) crystals after earlier work with NaI(Tl) and LSO, because CsI(Na) being less hygroscopic than NaI(Tl) is easier to work with and because of its lower cost and greater availability than LSO. Our choice of layer thickness was such as to provide a reasonably efficient multilayer stack with just a few layers. Our initial measurements and device characterization, reported here, are with a device with just 3 crystal layers; this resulted from our limiting the number of layers and the amount of multiplexing in the readout so as to study in detail the effects of multiplexing in depth.

II. Materials and Methods

A. Detector Configuration

Measurements were carried out with two detector modules operating in coincidence. Each module contained 3 layers of polished CsI(Na) scintillator, with each layer 3mm thick and having a 114mm x 114mm lateral extent. These crystal layers were polished first with a succession of sandpapers, then with Aluminum Oxide powders in mineral oil-based slurries. Crystal layers were alternated with perpendicular wavelength shifting fiber ribbons (Bicron BCF91A, 1mm diameter multiclad), with each ribbon 112mm in width and approximately 30cm in length. Each crystal layer was coated with a high-index (n=1.65) resin to provide provide an index matching layer between the crystal (n=1.82) and the outer cladding of fiber ribbon (n=1.42). Acrylic frames with 4mm thickness were used to assemble a multilayer stack of scintillator crystals alternating with fiber ribbons, and to hold depth-encoding Z fibers in position at two crystal edges.

After assembly, each multilayer stack was cast in clear epoxy (Emerson and Cummins Stycast 1267) and coupled to a 1" thick acrylic light mixer with the same epoxy. The two X and Y fiber ends opposite the fiber readout ends were optically coupled to plane mirrors (aluminized mylar) to increase the number of photons reaching the readout ends. The base of each module was optically coupled to a diffuse white reflector, as was the outside of each acrylic light mixer to increase the light yeild reaching the trigger PMTs.

Each module was coupled with optical grease (Dow Corning Q2-3067) to an Anger-type array of 4 Phillips XP3697/PA PMTs, each with a 60mm x 60mm envelope. Linear x10 preamplifiers (Phillips NE5205AN) were mounted on each photomultiplier's base to boost gains. Detector modules, the Anger PMTs, and fiber readout PMTs were mechanically mounted in a light-tight support structure with signal, high-voltage, and low-voltage feedthroughs.

Each 112mm fiber ribbon was split into 8 bands each containing 14 fibers. The 16 bands of X-fibers and the 16 bands of Y-fibers were grouped into 8 sets of 4-fold multiplexed bundles, with a pair of bands within a layer (lateral multiplexing) bundled with the corresponding pair from another layer (depth multiplexing). Each bundled set of 4 bands was held in a custom Delrin fiber vise, polished, and coupled with optical grease to a Hamamatsu R5900-L16 multianode photomultiplier. The 14mm bundle width ran across the discrete anodes of the multianode PMT, each of which corresponds to a 1mm x 16mm photocathode region. The 16 anodes of each multianode were then read out with 1D charge division: the sum of the charge division signals A1+A2 indicated the light yield from each bundle, while the normalized coordinate (A2-A1)/(A2+A1) measured the average lateral position of light across the bundle [5].

B. Data Acquisition Electronics

The signals from each Anger tube were split, with one copy used for triggering and the other delayed for ADC measurement. The 4 trigger signals from each detector module were analog summed, shaped, and discriminated; coincidences

between discriminated analog sums from the two modules provided triggers which generated ADC gates and initiated readout. Additional copies of each discriminated analog sum were sent to TDCs (LeCroy 2228A) for timing masurements.

Copies of the Anger signals, as well as all charge division signals from the fiber readout PMTs, were delayed by 200ns and digitized within 1microsecond gates by LeCroy 2249W ADCs. A total of 2 TDC channels and 47 ADC channels were read out through CAMAC for each event. Data was acquired with a PC through a custom PCI/CAMAC interface and controller obtained from the Budker Institute for Nuclear Physics in Novosibirsk, Russia. This interface was able to collect triggers at a rate of several hundred Hz, which was sufficient for the phantom studies described below. We are currently developing a higher-rate interface for clinical use.

C. Event Reconstruction

All fiber readout PMTs were calibrated to give the number of photoelectrons collected from each fiber bundle on each event, which was greatly facilitated by the excellent single photoelectron pulse height distribution of the R5900-L16 PMTs. For each event, the X- and Y- bundles with the most light were identified, and the Anger and depth information used to demultiplex and identify which of 4 bands within a bundle produced the signal. The Anger system spatial resolution was sufficient such that the demultiplexing was quite unambiguous. The charge division information from the selected X- and Y- fiber readout PMTs were then converted to coordinates across each fiber ribbon and combined with the position of each fiber ribbon within the apparatus to give global X-, Y- and Z- coordinates.

Analytic single-pass 3D reconstruction is impossible for the limited-angle geometry of two parallel detector plates (as required by the physical contraints of PEM), since the geometry does not satisfy Orlov's criterion. Nonetheless, 3D information is present in the parallax of oblique rays, and can be exploited through iterative reconstruction algorithms. We have used an Inverse Monte Carlo algorithm [6] loosely based on ML/EM but operating in image space, and have used all triggered events[7]. The essence of this algorithm is that collected events are back-projected across a 3D voxel array, and this back-projected data is then iteratively compared with back-projected "pseudo-data" generated by Monte Carlo simulation of the hypothesized source distribution at each step [8]. This algorithm rapidly accomplishes most of its convergence, and 5 iterations were used in this work. Reconstruction times for these datasets were comparable to acquisition times when performed on a simple single-processor workstation.

D. Phantoms

The first phantom we imaged, which was manufactured by North American Scientific and provided for our use by PEM Technologies, Inc., consisted of two hot-spot inserts surrounded by a uniform background as illustrated in Figure 2. This was accomplished by filling a 17cm diameter by 6cm height cylinder with uniform Ge-68 activity distributed throughout an epoxy base; an 18mm diameter hollow tube traversing the cylinder accomodates inserts with activity concentrations 10X the background and volumes of 1.0 and 0.5cc each. The total activity was 10 μC.

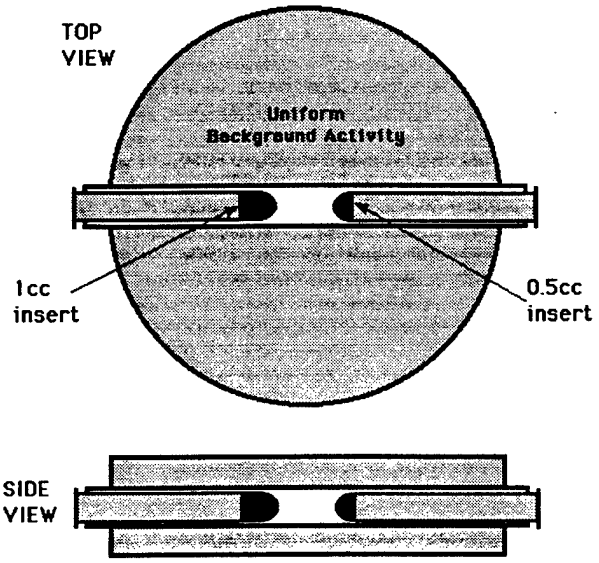

Figure 2: Hot-spot phantom with two inserts surrounded by uniform background activity. The activity concentration of the hot spots was 10x the activity concentration of the uniform background.

The second phantom we imaged was of our own construction, and is illustrated in Figure 3 below. It consisted of a 3.5mm thick acrylic piece perforated by the hole pattern

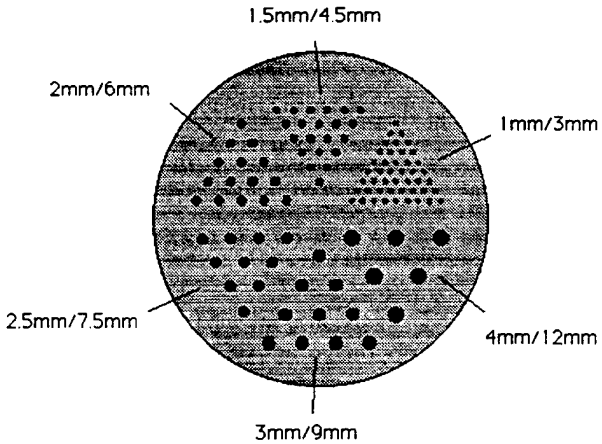

Figure 3: Hot-spot resolution phantom. Spots with diameters of 4mm, 3mm, 2.5mm, 2mm and 1mm have separations of 3 times their diameters.

shown, sandwiched between two 0.25mm thick layers of uniform activity. The 3.5mm thick insert was placed within a 4mm height cylinder and filled with F-18 in an aqueous solution. The effect is to produce hot-spots with an activity/background ration of 8:1; the initial activity of this

phantom was 30μCi distributed in a volume of 1.3 cm cubed. Both the first and second phantoms were oriented with their narrowest dimension normal to the two detector planes, and with their geometrical center mid-way between the two planes.

The third phantom which we imaged consisted of two hypodermic needles (8cm length x <1mm ID) containing F-18 in an aqueous solution, mounted perpendicular to each other and lying within two parallel planes separated by 14mm; these planes were then oriented parallel to the two detector planes, with one of the two planes passing through the point mid-way between the two detector planes. The initial activity of this phantom was also about 30μCi.

III. Experimental Results

A. Detector Performance

Detector system performance was measured in response to the third phantom; separate measurements tested performance of the Anger energy/trigger/timing subsystem and of the fiber coordinate measurement subsystem. The Anger PMTs within each module were calibrated with an LED to determine the approximate number of photoelectrons per ADC bin, taking the event-to-event fluctuations in response to the LED as entirely due to photostatistics. Figure 4 below shows the energy resolution (i.e. the ADC sum for the 4 Anger PMTs within a module, after calibration) and the Anger system light yield in photoelectrons. The energy resolution obtained *at trigger level* for those events which generated a trigger was better than 20%, including nonuniformities in detector response both laterally (e.g. less light was collected from the detector corners) and in depth. It should be noted that information on event positions both laterally and in depth is available on an event-by-event basis, so that the obtainable *offline* energy resolution is significantly better than that shown. The low-energy tail of our trigger senstivity reflects the limitations of the very simple shaping circuit used. The timing performance for two detectors in coincidence is shown in Figure 5, demonstrating 25ns FWHM time resolution.

The fiber coordinate measurement achieved nearly 3mm FWHM spatial resolution in response to a line source within the third (needle) phantom, with the long tails resulting from the presence of the second line source outside the focal plane as shown in figure 6. Measurements with a point source showed better spatial resolution, approaching 2mm FWHM when restricted to one small section of one module coincident with another small section on the opposing module. We attribute this to variations in crystal surface finish and some fiber readout calibration errors. The average fiber light yield for the fiber band with most photoelectrons in a photopeak event was 10 photoelectrons, as shown in Figure 7.

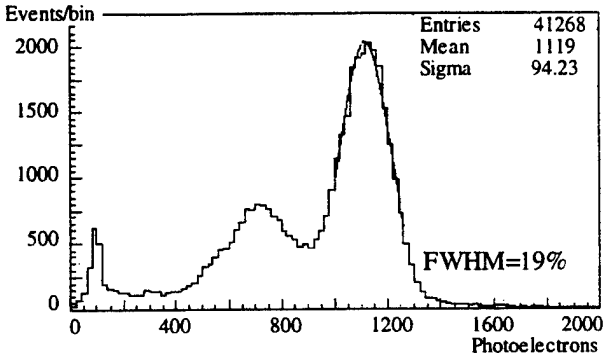

Figure 4: Collected light distribution (in photoelectrons) *at trigger level* for the analog sum of 4 Anger PMTs within a detector module. The photopeak is clearly visible and easily selected by a simple threshold trigger circuit.

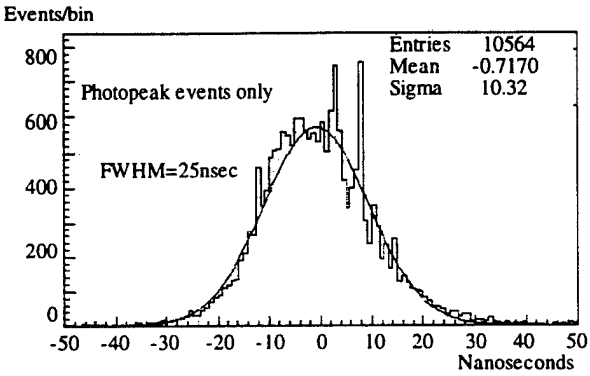

Figure 5: Time difference (in nanoseconds) between signals from discriminated anode sums for two coincident detector modules.

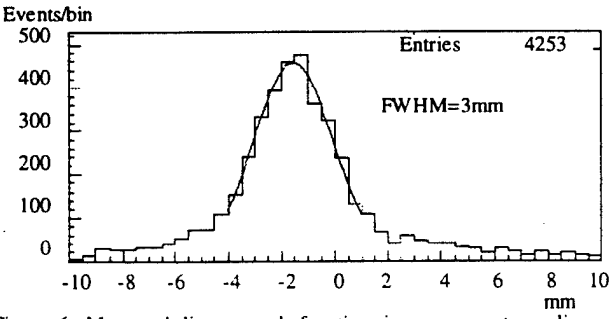

Figure 6: Measured line spread function in response to a line source spanning nearly the width of the field of view.

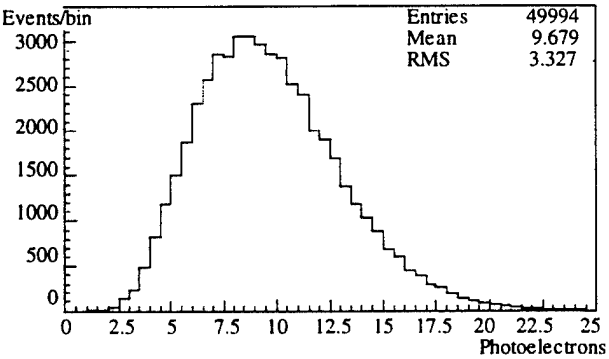

Figure 7: Measured light yield distribution (in photoelectrons), for one end of one fiber bundle as read out through one multianode photomultiplier.

B. Phantom Images

The image reconstructed from data collected with the hot-spot phantom illustrated schematically in Figure 2 is shown in Figure 8 below. Both the 1cc and 0.5cc hot-spots are clearly distinguished from the uniform background, with this image reconstructed from about 100,000 photopeak-photopeak events. The detector separation was >10cm due to some mechanical constraints, but the depth-of-field resolution achieved in nonetheless quite good. The geometric acceptance for coincidence events falls nearly linearly with distance from the device edge, so that edges and corners of the image are more susceptible to statistical fluctuations. Nonetheless, with just 100K events, a single threshold is sufficient to eliminate all activity outside the hot-spots throughout the field of view, as shown in the 3-D rendering at the bottom half of Figure 8.

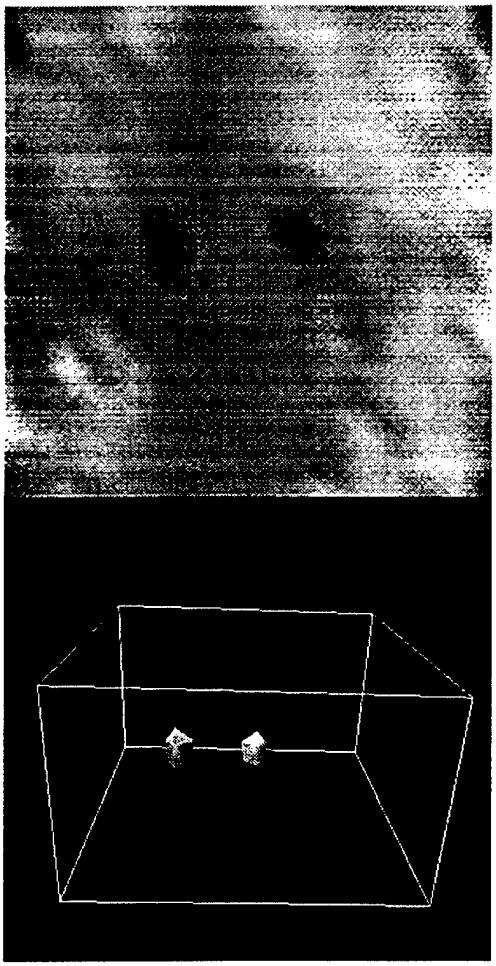

Figure 8: Reconstructed image of the hot-spot phantom with uniform background activity (See Figure 2). The top image shows a cross-sectional slice of the object through the 11cm x 11cm plane mid-way between the two detectors. The hot-spot activity is 10x that of the uniform background, and the hot-spot volume is 1.0cc (left) and 0.5cc (right). The bottom image shows a 3-dimensional rendering (rendered by the Silicon Graphics "Explorer" program) of the activity distribution above a fixed threshold. No activity outside the hot-spots survives the threshold cut.

The image reconstructed from data collected with the hot-spot resolution phantom illustrated schematically in Figure 3 is shown in Figure 9 below. The 4mm, 3mm, and 2.5mm hot-spots are completely resolved, as are some are of the 2mm hot-spots. The total number of events is again about 100K.

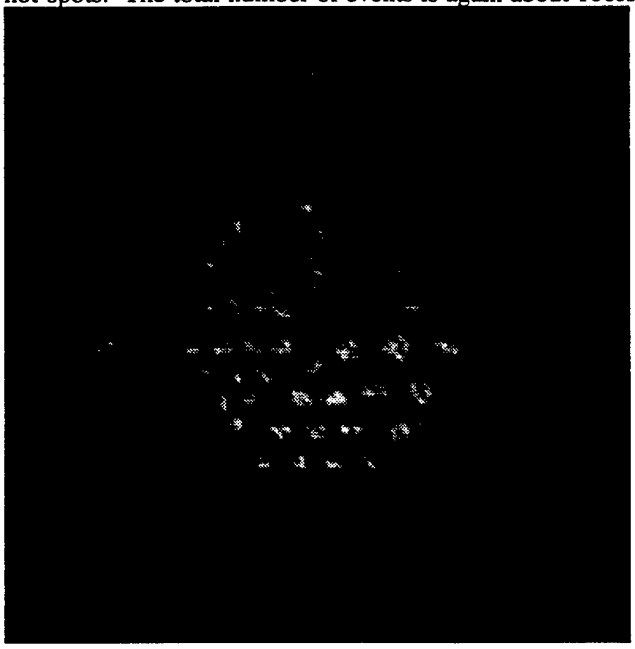

Figure 9: Reconstructed image of the hot-spot resolution phantom (See Figure 3). The phantom's hot-spot/background activity ratio was 8:1.

The image reconstructed from data collected with the two-needle phantom is shown in Figure 10 below. The spacing between the two detector planes was 9cm, and the two needles are easily resolved in depth. The number of photopeak-photopeak coincident events used was about 70K.

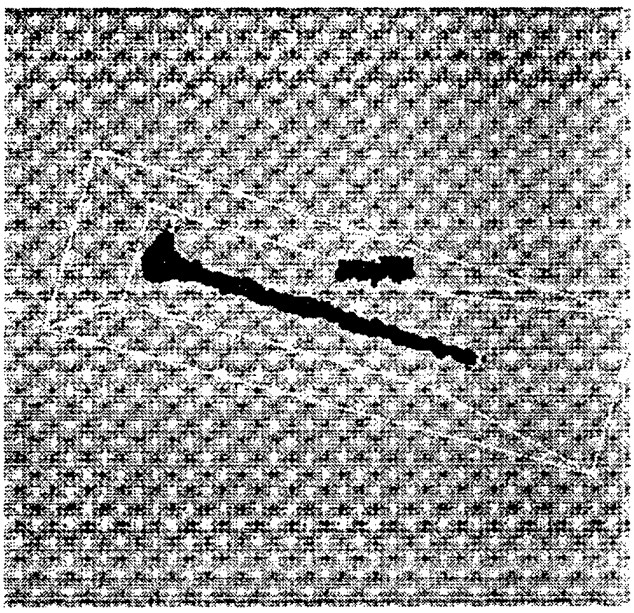

Figure 10: Reconstructed image of two perpendicular hypodermic needles, each in a plane parallel to the detector planes, and with the two needle planes separated by 14mm. They are well-resolved in the depth-of-field.

IV. Discussion

Separation of functions between energy/trigger/timing (with the Anger array) and interaction coordinate measurements (with the wavelength-shifting fiber readout) allows their separate optimization. High spatial resolution results from small single crystal layer thickness, while high efficiency results from a large total crystal thickness. Separate optimization thus requires the capability to preserve Anger system performance in a device with a large number of layers. The initial studies reported here indicate the capability of 3-layer modules, and we are continuing this work on modules containing more crystal layers. Preliminary measurements have shown good energy resolution at the trigger level for 7-layer modules, when adequate care is taken in crystal surface treatment. The quality of the crystal surface polish is critical both to the fiber coordinate measurement and to the Anger energy/trigger function. For the fiber coordinate measurement, it determines the degree to which photons spreading and totally internally reflecting away from the interaction point are able to exit the crystal and enter fibers before reaching the crystal edge. For the energy measurement, it determines the overall transparency of a multilayer crystal/fiber stack to wavelength-shifted light which is not piped down fibers. Although CsI(Na) is soft, it is somewhat hygroscopic and difficult to polish well, which we believe contributes significantly to the limits on our device's spatial resolution.

Other scintillator material properties which affect the detector performance are its density and its photofraction. A Compton scatter interaction where the secondary gamma is converted elsewhere within the detector will produce an Anger signal which lies within the photopeak. Right-angle Compton scatters which convert in the same crystal plate are indistinguishable from photocaptures, but result in distributed light production within the scintillator crystal and thus positioning errors. Positioning errors due to detector Compton scattering are lessened when using a scintillator with a higher photofraction, and a denser scintillator can be used to decrease the number of layers and/or to decrease layer thickness while maintaining detector efficiency. All these reasons, in addition to its greater speed relative to CsI(Na), make LSO an excellent material for very high-performance wavelength-shifting fiber readout modules. We have recently acquired more significant amounts of this material and are proceeding to develop new modules containing LSO in the near future.

One major advantage which CsI(Na) modules maintain relative to LSO modules is the much lower cost and greater availability of CsI(Na). For that reason, we are also planning to construct devices with significantly larger fields of view using this relatively inexpensive scintillator material. The cost of wavelength-shifting fiber readout scales proportional to the perimeter of the device, so that larger areas can be covered quite cost-effectively. Rate capability issues are significant for larger devices, but the great gain in efficiency relative to thin crystals (such as in commercial dual-plane coincidence imagers) shows potential for significant performance gains.

V. Conclusions

We have constructed and tested two multilayer CsI(Na) PET detector modules with wavelength-shifting fiber readout, and have used them to image several phantoms. Wavelength-shifting fiber readout has intrinsic depth-of-interaction sensitivity, which is important when scintillators are brought into close proximity to an object being imaged. With depth-of-interaction sensitivity, the parallax information in oblique incident rays can be used to resolve objects in the depth-of-field, as we have demonstrated. In a two-plate detector geometry this requires iterative reconstruction techniques and limited-angle tomography; and we have shown that this is feasible for a device applicable to Positron Emission Mammography (PEM). Finally, the materials used to construct our test device were relatively inexpensive, and the device design scales to larger sensitive areas cost-effectively.

VI Acknowledgment

We would like to thank Dr. Irving Weinberg of PEM Technologies, Inc., for the use of his hot-spot phantom with uniform background activity. We would also like to thank Dr. Jack Correia of the Massachusetts General Hospital for his gracious assistance in supplying us with F-18 for our phantom studies. Finally, we would like to thank Dr. Joseph Ferrucci and Dr. Victor Lee of the Boston Medical Center's Department of Radiology for helpful discussions.

* This research was supported by US Army Medical Research and Material Command Breast Cancer Research Program Grant #DAMD17-96-1-6192 and in part by the Commonwealth of Massachusetts Department of Public Health Breast Cancer Research Program Grant #SC-DPH-3408-799D049

VII References

[1] W. Worstell, S. Doulas, O. Johnson, and C.-J. Lin, "Scintillator Crystal Readout with Wavelength-Shifting Optical Fibers", *Proc. IEEE 1994 Med. Imag. Conf.*, 1869-1873.

[2] W. Worstell, O. Johnson, V. Zavarzin, "Development of a High-Resolution PET Detector using LSO and Wavelength-Shifting Fibers ", *Proc. IEEE 1995 Med. Imag. Conf.*, 1756-1760.

[3] Thompson CJ, Murthy K, Weinberg IN, Mako F: "Feasibility Study for Positron Emission Mammography", *Med. Phys.* 21:4, 529-537 (1994).

[4] Thompson CJ, Murthy K, Clancy RL, Robar JL, Bergman A, Lisbona R, Loutfi A, Gagnon JH, Weinberg IN, Mako R, "Imaging Performance of PEM-1: A High Resolution System for Positron Emission Mammography", *Proc. IEEE 1995 Med. Imag. Conf.* 1074-1078.

[5] D. Grigoriev, O. Johnson, W. Worstell and V. Zavarzin, "Characterization of a New Multianode PMT for Low level Optical Fiber Readout", ", *Proc. IEEE 1996 Med. Imag. Conf.* 638-641.

[6] Floyd, C, Jaszczak R, Coleman E, "Inverse Montecarlo: A Unified Reconstruction Algorithm for SPECT", *Trans. on Med. Imag.* 32:779-785 (1985).

[7] Witherspoon M, Muehllehner G, "An Iterative Image Space Reconstruction Algorithm Suitable for Volume ECT", *IEEE Trans. Med. Imag.* 5:61-66(1986).

[8] W. Worstell, H. Kudrolli, V. Zavarzin, "Monte Carlo-Based Implementation of the ML-EM Algorithm for 3-D PET Reconstruction", unpublished, submitted to *IEEE Trans. Med. Imag.*

An Inverse Monte Carlo Algorithm for 3-D PET Image Reconstruction [1]

H.Kudrolli[2] , W.Worstell[2] *Member, IEEE* and V.Zavarzin[3]
[2]Boston University Physics Department and Center for Photons. 590 Commonwealth Avenue, Boston, MA 02215
[3]Tomotronics, Inc. 5 Snake Brook Road. Wayland, MA 01778-5013.

Abstract

We have developed a 3D PET reconstruction algorithm based upon Inverse Monte Carlo analysis and have tested it on data acquired by high-resolution 3D PET detectors. This algorithm back-projects 3D PET data across a 3-dimensional array of voxels, then during each iteration generates Monte Carlo "pseudo-data" which is similarly back-projected across a 3-dimensional voxel array. Comparison between the back-projection of the data and the back-projection of the pseudo-data is used to update the source distribution hypothesis. Inverse Monte Carlo methods provide a natural framework for incorporation of detector response functions, and potentially for the incorporation of effects due to scatter and other sources of systematic error. The algorithm is fairly fast, capable of reconstructing a 128 x 128 x 128 Hoffman brain phantom image in a few hours on a modern single-processor workstation. We have achieved nearly linear speed-up by implementation of the algorithm on a computer with 8 parallel processors.

I. Introduction

The recent trend in operating PET detectors in three-dimensional mode, to achieve higher sensitivity, has aroused interest in 3D image reconstruction algorithms. The requirements for such algorithms is that they have to be quantitatively accurate, as well as, have fast reconstruction times. The 3DRP algorithm proposed by Kinahan and Rogers [1] is most commonly implemented on commercial PET scanners. This algorithm is robust and has good image contrast but suffers from poor noise properties and treatment of statistical data. The ML-EM algorithm [2, 3, 4], widely applied in the 2D tomography is computationally cumbersome in 3D. The ML-EM algorithm is an iterative algorithm, which requires calculation of the system response matrix.This is the matrix of probabilities that a photon emitted from a certain point will be detected in a particular detector line of response. This probability matrix is usually too huge to store in memory and has to be either stored in on disk or calculated on the fly. Several groups have used symmetries and sparseness of this matrix to be able to store it in memory [5]. Hudson and Larkin proposed OS-EM algorithm [6] which uses symmetries in the data to speed up the iterations but still quite slow in 3D. Gaining popularity for 3-D reconstruction are the approximate rebinning algorithm like the FORE algorithm which rebins data into set of 2D slices. The rebinned slices can be reconstructed using filtered backprojection or ML-EM, OS-EM or WLS methods [7].These algorithms are computationally fast but the accuracy of the reconstructed images is limited by the approximations implicit in the line integral model.

Our interest in image reconstruction arises from development of a unique detector made wavelength shifting fibers [8]. This has 2 large planar detectors facing each other the position coordinates for the detected events are readout by 1mm fibers and our detector has a spatial resolution of 2-3mm. Design considerations, especially for mammogarphy, prohibits construction of a detector geometry with complete angular views. This incomplete set of projections excludes the possibility of using FBP as they do not satisfy Orlov's criteria [9]. ML-EM algorithms which is not restricted to device geometry is a possibility but the computational burden associated with explicitly calculating the system response function makes it impartical. Thus we felt a need for a new algorithm which would work for a limited angle geometry detector which could generate fast 3D images.

Our algorithm is based on Monte Carlo method and it solves the Inverse problem of solving for the source distribution given the data from the source distribution. Monte Carlo method for solving for source distribution has been proposed more than 10 years ago for SPECT imaging [10]. Monte-Carlo methods ,however, have been used in PET to study the effects of attenuation and scatter.

This algorithm is, however, not restricted to a dual plane geometry but can be applied to a wide range of detector geometries. We will present its implementation on a two high resolution detectors with very different detector geometries.

II. Theory

The Inverse Monte Carlo algorithm is an iterative algorithm which updates a hypothesized source distribution. It does this by Monte Carlo sampling from the source distribution and comparing it with the acquired data. The algorithm digitizes the image space into voxels and starts with first estimate for the source distribution.Monte Carlo events are generated from the first estimate according to the activity of the source distribution in the voxel. In other words, photon pairs are generated from a from a random point within the voxel and given a random direction. This photon pair is forward projected to find if they hit the detector. If they hit the detector then the event is backprojected Backprojection is done similar to the method described by Barresi [11].

This algorithm is similar to the image space reconstruction algorithm (ISRA) proposed more than 10 years ago by Daube-

[1]This research was supported by US Army Medical Research and Material Command Breast Cancer Research Program Grant DAMD17-96-1-6192 and in part by the Commonwealth of Massachusetts Department of Public Health Breast Cancer Research Program Grant SC-DPH-3408-799D049.

Witherspoon and Muehllehner [12] in that the measured data is stored in the backprojected array. Also comparison of the data and simulated data is done in backprojection space.

The difference between the backprojection of the data and the backprojection of the simulated data is used to update the image hypothesis. In the following iterations the number of events from a voxel generated is equal to the difference between the two backprojections at that voxel. The events that are subsequently generated are similarly projected to find where they hit the detector and then backprojected.However, if the simulated backprojection at the source voxel is less than the measured backprojection at that voxel then the backprojection is added. In the case that the simulated backprojection is more than the measured backprojection the backprojection is subtracted.

For the choice of first estimate for source distribution, we can start with a uniform source or image formed from some earlier iteration. Also we can also take the backprojection of the data as the first estimate and it has been seen that this is a very good starting point.

We have worked with a stopping criteria that the number of events generated is about 10 times the number of events detected. We have assumed this without proof but we have discovered empirically that the image quality does not improve significantly for more events generated.

III. Implementation of Algorithm for 2 Plane Geometry

A. *Software phantom studies for BU PET geometry*

The algorithm was tested on simulated phantom setup with the detector model based on the detector prototype that has been fabricated in our lab [8]. The detector geometry consisted of 2 parallel plates each 11cm x11cm , separated by 6 cm as illustrated in Fig 1. This detector resolution was taken to be 2 mm.

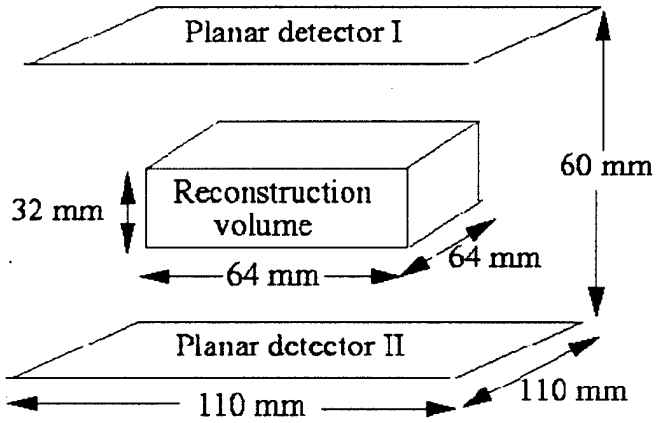

Figure 1: Schematic illustration of the Boston University PET detector.There are only 2 planar detectors of size 11 cm x 11 cm facing each other. The distance of separtion can be varied.

We simulated 20 million events with an array of 64x64x32 voxels each 1mm x 1mm x 1mm with Poison fluctuations. We include 3 hot spots with 8 times background intensity; these cylinders are 10mm,8mm and 6mm in diameter and lengths 1.5 times their diameter. The cylinders will be reffered to as cylinders A,B and C. This software phantom was chosen to match that used in a previously published work for Positron Emission Mammogarphy [13]. Cylinders A and B lie in the same Z plane and can be seen in the same slice as shown in fig 2 (1,2).

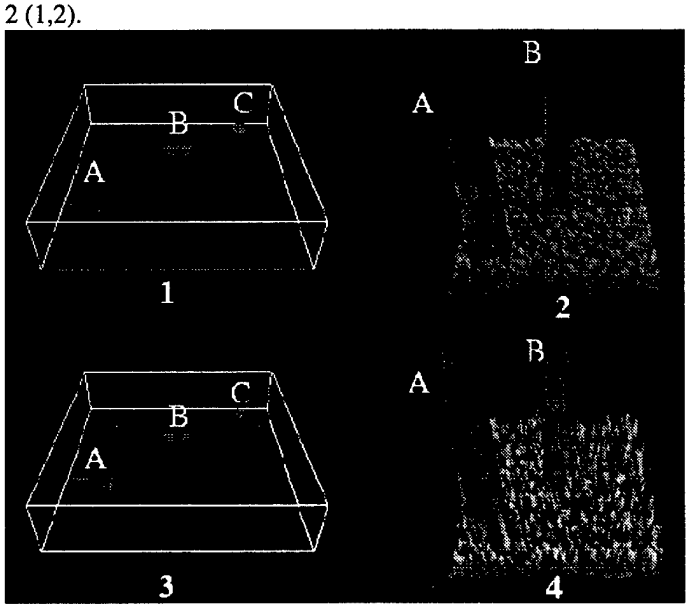

Figure 2: (1) 3D rendering of the simulated phantom with three cylinders-A,B,C. (2)Slice through one plane showing relative intensity of cylinders A and B versus the background 8:1. Note cylinder C is on another plane and cannot be seen.(3)3D rendering of the reconstructed image.(4)Slice through one plane of reconstructed image showing relative intensity of cylinders A and B versus background.

The images shown in Fig 2 (3,4) was reconstructed in 25 iterations. The convergence of the algorithm is illustrated in fig 3. This image was reconstructed in less than 10 minutes when implemented in a SGI/Cray Origin 2 Series computer with a 192 MIPS R10000 processor running at 195 MHz.

B. *Phantom studies with actual data from BU PET*

A number of objects were imaged and reconstructed using our 3 layer CsI(Na) prototype detector. This work has been published in an earlier work regarding work regarding the performance of the detector and so will not be reproduced here[8].

IV. Data from Ring Detector Geometry

This algorithm was tested on data taken by the HEAD PENN-PET detector of the Hoffman brain phantom. The HEAD PENN-PET scanner is a volume-imaging PET scanner without inter-plane septa with high spatial resolution and sensitivity [14]. The spatial resolution is 3.5 mm in both transverse and axial directions in the center of the field of view (FOV). The FOV is 25.6 cm in both transverse and axial directions.

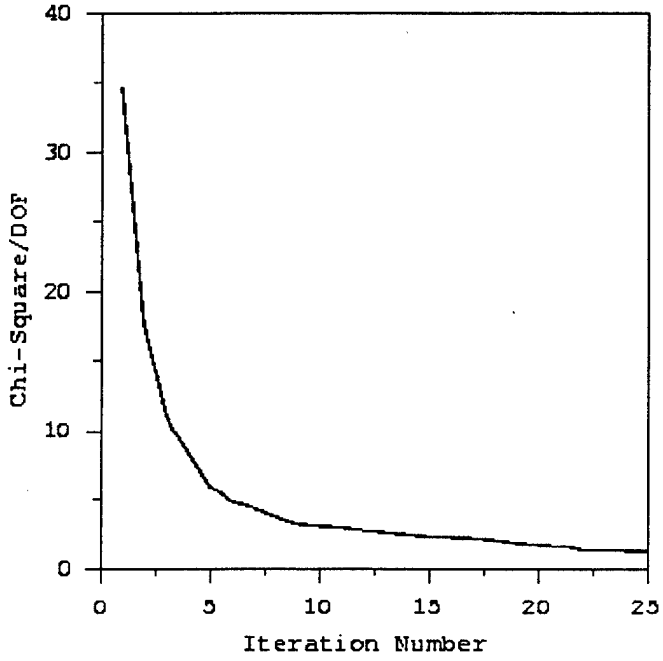

Figure 3: The Chi-Sq convergence rate versus number of iterations

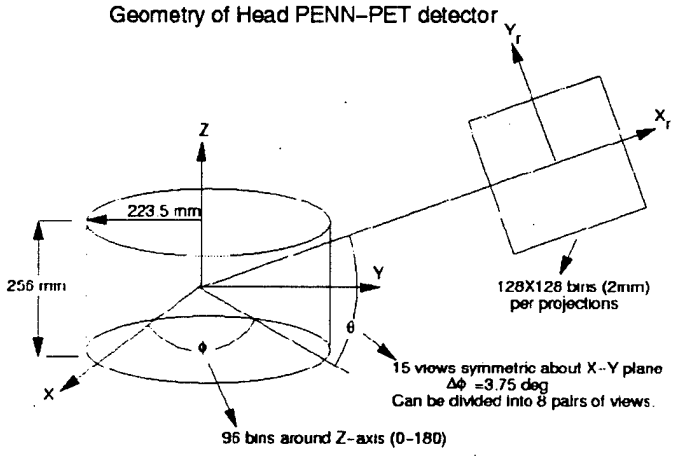

Figure 4: Schematic illustration of geometry of HEAD PENN-PET detector The 15 theta projections can be paired into 8 sets of projection views symmetric about the XY plane.

A. *Format of the data*

The data is stored into four-dimensional projection matrices (x',y',phi,theta) that are 128x128x96x15. The spatial sampling is 2mm. The data had been normalized for efficiency, detector non-uniformities and attenuation corrected.

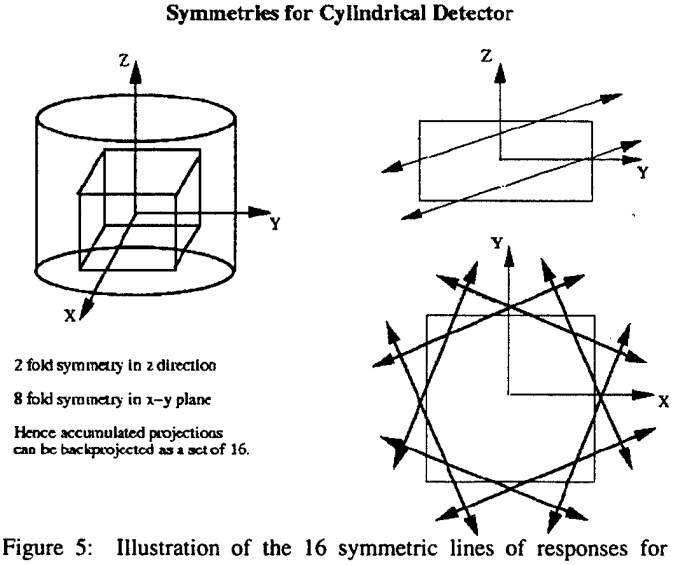

Figure 5: Illustration of the 16 symmetric lines of responses for cylinderical detector geometry and rectangular reconstruction volume

B. *Symmetries*

The four dimensional projection matrix which is approximately 46 MBytes is too huge to fit into memory for most computers. Implementation of the algorithm for this data set was done by using the symmetries presented by the cylindrical geometry of the detector. The projection data was divided into 8 sets of projections such that each set of projection would lie within 2 symmetrical projection views about the XY plane as illustrated in Fig 4. The algorithm was modified such that it would loop through the 8 projection views. For each projection view the events generated from the source distribution were confined to a limited theta angle range such that they fell within that projection view. The simulated events were forward projected and accumulated in a 128 x 128 x 96 x2 projection matrix. For each projection view backprojection was done once all the events were generated and forward projected and accumulated. By accumulating the projection and backprojecting simultaneously we could use the 16 symmetries in the lines of responses Fig 5 to give a linear speed up.

C. *Parallel Implementation*

Since the projection data was be split into 8 projection views this algorithm could easily parallelized by 8 processors such that one processor reconstructs 1 projection view. This was implemented on a a SGI/Cray Origin2 Series parallel computer system with multiple processors. Each processor was a 192 MIPS R10000 running at 195MHz. The algorithm was written

in Fortran and the parralelization was done by using Message Passing Interface (MPI).

D. Results

Data the Hoffman Brain Phantom were reconstructed by this algorithm . The total number of attenuation corrected events in this data were about 800 million. Using 4 mm size voxels the image were reconstructed in 25 iterations within 15 minutes while simulating 3 billion events,Fig 6. Using the same number of iterations and simulated events but using 2mm voxel size the reconstruction time was 100 minutes.Fig7.

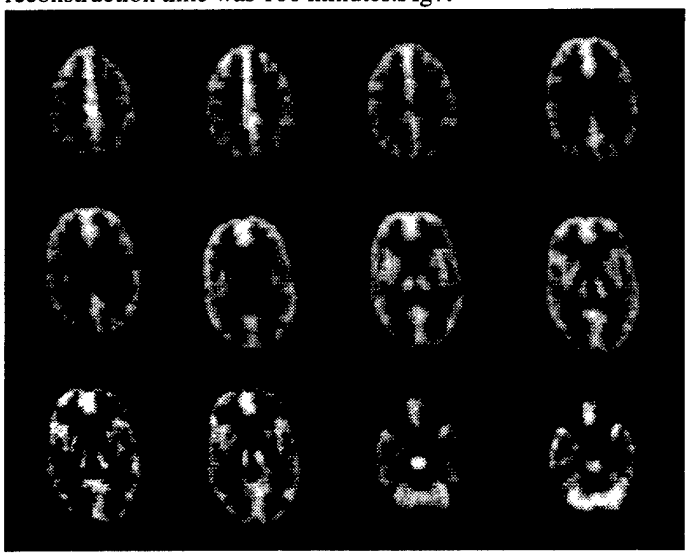

Figure 6: Hoffman Brain Phantom using 4 mm voxel size; using 25 iterations and simulating 3 billion events

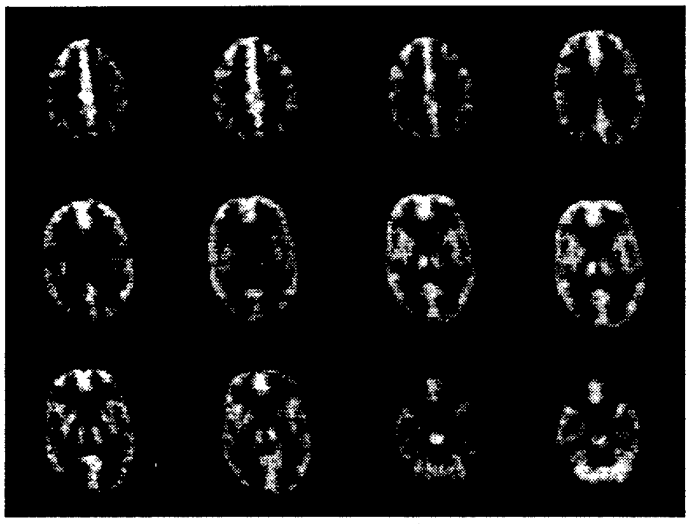

Figure 7: Hoffman Brain Phantom using 2 mm voxel size ;using 25 iterations and simulation 3 billion events

V. Discussion

The images from the 2mm voxel size had higher contrast but were noisier that produced by using 4 mm voxel size. The image quality does not look remarkedly different but this is due to the effects of detector resolution which is 3.5 mm. To deconvolve the effects of detector we will reconstruct images from the digital Hoffman brain phantom. The effects of the number events to be simulated as a function of voxel size will be studied using this phantom [15].

VI. Conclusion

We have explored the possibility using Inverse Monte Carlo methods for image reconstruction and applied it to data from 2 high resolution detectors with very different geometries. The algorithm is shown to give qualitatively accurate images of complex phantoms. Precise quantitative analysis of the algorithm will be done next using the EVAL3DPET software developed by the Medical Image Processing group at the University of Pennsylvania [16, 17].

VII. Acknowledgments

The authors would like to thank Dr. Joel Karp and Dr. Lars-Eric Adams, from University of Pennsylvania for providing us with the data for the Hoffman Brain phantom, and also for their helpful suggestions. We would also like to thank Ghislain Airieau for useful disscussion on implementation of the algorithm.

VIII. References

[1] Kinahan P.E and Rogers J.G "Analytic three-dimensional image reconstruction using all detected events" *IEEE Trans. on Nucl. Sci.*,vol. 36,pp.964-968,1990

[2] Shepp L.A. and Vardi Y. "Maximum likelihood reconstruction in poistron emission tomography" *IEEE Trans on Med. Imag.*,vol.MI-1,pp.113-122,1982.

[3] Lange K. and Carson R. "EM reconstruction algorithms for emission and transmission tomography." *J.Comput. Assist.Tomography.*,vol.8,pp.306-316,1984

[4] Lewitt R and Muehllehner G. "Accelerated iterative reconstruction for positron emission tomography based on the em algorithm for maximum likelihood estimation." *IEEE Trans. on Med. Imag.*,vol. MI-5.pp.16-22,1986

[5] Qi J, Leahy R.M, Hsu C, Farquhar T.H, Cherry S.R "Fully 3D Bayesian image reconstruction for the ECAT EXACT HR+" *IEEE Trans. on Nucl. Sci.*,vol. 45,pp.1096-1103,1998

[6] Hudson H.M. and Larkin R.S. "Accelerated image reconstruction using ordered subsets of projection data" *IEEE Trans. on Med. Imag.*,vol. MI-13,pp.601-609,1994

[7] Defrise M,Kinahan P.E, Townsend D.W, Michel C, Sibomana M. and Newport D.F "Excat and approximate rebinning algorithms for 3-D PET data" *IEEE Trans. on Med. Imag.*,vol. 16,pp. 145-158,1997

[8] Worstell W. Johnson O, Kudrolli H, Zavarzin V. "First results with high-resolution PET detector modules using wavelength-shifting fibers" *IEEE Nucl. Sci. Sym. Conf. Records,Albuquerque*Cat. No. 97CH36135,1997

[9] Orlov S.S "Theory of three-dimensional image reconstruction. I Conditions for a complete set of

projections." *Soviet Physics Crystallography* vol 20(4),pp.429-433,1976

[10] Floyd C.S and Jaszczak R.J, "Inverse Monte Carlo: A unified reconstruction algorithm for SPECT." *IEEE Trans. on Nucl. Sci.*,vol. 32,pp.779-785,1985

[11] Barresi S, Bollini D, and Del Guerra A, "Use of a transputer system for fast 3-D image reconstruction in 3-D PET" *IEEE Trans. on Nucl. Sci.*,vol. 37,pp.812-816,1990

[12] Daube-Witherspoon M.E and Muehllehner G, "An iterative image space reconstruction algorithm suitable for volume ECT" *IEEE Trans. on Med. Imag.*,vol. MI-5,pp.61-66,1986

[13] Thompson C.J, Murthy K, Picard Y, Weinberg IN, and Mako F. "Positron Emission Mammogarphy (PEM): A promising technique for detecting breast cancer" *IEEE Trans. on Nucl. Sci.*,vol. 42,pp.1012-1016,1995

[14] Karp J.S, Freifelder R, Geagan M.J, Muehllehner G, Kinahan P.E, Lewitt R.M Shao L. "Three-dimensional imaging characteristics of the HEAD PENN-PET scanner" *Jour. of Nucl. Med.*,vol. 38, No. 4,pp. 636-642,1997

[15] Hoffman EJ, Cutler PD, Digby WM, Mazziotta JC. "3-D Phantom to Simulate Cerebral Blood Flow and Metabolic Images for PET." *IEEE Trans. Nucl. Sci.*,vol. 37,pp. 616-620, 1990.).

[16] Furuie S.S, Herman G.T, Narayan T.K, Kinahan P.E, Karp J.S, Lewitt R.M and Matej S. "A methodology for testing statistically significant differences between fully 3D PET reconstruction algorithms" *Phys. Med.Biol.*,vol. 39,pp.341-354,1994

[17] Matej S, Herman G.T, Narayan T.K,Furuie S.S, Lewitt R.M and Kinahan P.E. "A methodology for testing statistically significant differences between fully 3D PET reconstruction algorithms" *Phys. Med.Biol.*,vol. 39,pp.355-367,1994

3-D Iterative Reconstruction Procedures for PET Detectors with Fixed Dual-Plane Geometry [1]

W.Worstell[2] H.Kudrolli[2], and V.Zavarzin[3]
[2]Boston University Physics Department and Center for Photonics. 590 Commonwealth Avenue, Boston, MA 02215
[3]Tomotronics, Inc. 5 Snake Brook Road. Wayland, MA 01778-5013.

Abstract

We have been developing 3D reconstruction procedures for detectors with a fixed dual-plane acquisition geometry, and in particular for Positron Emission Mammography (PEM) detectors. Because this limited-angle acquisition geometry does not satisfy Orlov's criterion, Fourier-based analytic reconstruction algorithms may not be used. Nonetheless, depth-of-field (tomographic) information is present in the parallax of oblique lines-of-response, and may be recovered using 3D iterative reconstruction techniques. The mapping of a 3D source volume onto a 4D line-of-response array requires a 7D system response matrix, which is at the same time inordinately large and sparsely populated. We have taken advantage of translational symmetries for detector acquisition planes parallel to planes of voxels, and have stored only non-zero system response matrix elements as a list. As a result, we are able to store pre-calculated system response matrix elements for a 36 x 36 x 40 voxel array sandwiched between two parallel 18 x 18 arrays of detector crystals in less than 4 Megabytes of memory. Because these matrix elements easily fit in computer memory, a full EM iteration requires less than 10 CPU minutes on a single-processor workstation. We are currently examining EM, OSEM and ISRA 3D iterative reconstruction algorithms using this compressed system matrix.

In addition to direct application of the system matrix during forward- and back-projection steps in each of the above algorithms, it is possible to approximate these steps using Monte Carlo sampling techniques. These "Inverse Monte Carlo" methods use an implicit form of the system response matrix contained within the Monte Carlo simulation of the source and detector systems. In the context of a dual plane acquisition geometry we are therefore able to compare the speed and accuracy of Inverse Monte Carlo and direct system matrix application techniques, in particular as a function of the number of detected events. Results of quantitative performance measures using simple software phantoms are presented, as well as results using data from real detectors and phantoms.

I. INTRODUCTION

Iterative reconstruction methods are widely used in Emission Computed Tomography (ECT) to more accurately incorporate source and detector system response information, and to more accurately treat event statistics, than is possible with less computationally burdensome analytic reconstruction methods [1]. Iterative techniques have been much more widely used in 2D rather than 3D acquisition geometries [2], because the resulting system response matrix is 4-dimensional for 2D acquisition (a 2D array of lines-of-response for each source element) and 7-dimensional for 3D acquisition (a 4D array of lines-of-response for each source element). Direct storage of a 7D array with any reasonable number of voxels and lines-of-response is usually impractical, even after array compression to save only non-zero elements and application of system symmetry operations [3]. Recently, methods have been developed to rebin 3D data as a set of nearly equivalent 2D projections, but these operations inevitably trade off some spatial and statistical accuracy for the considerable computational advantages of parallel 2D rather than fully 3D reconstruction.[4]

We have been interested in the application of Monte Carlo sampling techniques to the forward- and back-projection operations required in 3D iterative reconstruction algorithms, where the information which might be stored *explicitly* in the system response matrix is embedded *implicitly* in the Monte Carlo system simulation model. This allows for fully 3D reconstruction with no re-binning and accurate modelling of the statistical properties of the data. Such methods have the further attractive feature of potentially incorporating a detailed model of the source (e.g. attenuation, scatter) and detector system (e.g. resolution, depth-of-interaction, detailed geometry) properties. The computational burden associated with such modelling is less than it might at first appear (when efficiently coded), and it becomes less burdensome as more computer power and/or parallel processing capability becomes available.

Our group's interest in 3D iterative reconstruction techniques grew out of our need for tomographic image reconstruction capability in a limited-angle data acquisition geometry, in particular for application to a Positron Emission Mammography (PEM) detector [5]. This device has a fixed dual-plane acquisition geometry, acquiring depth-of-field information along the axis between the two detector planes in the form of parallax between views along different oblique lines-of-response. Analytic reconstruction techniques are ruled out because this limited-angle acquisition geometry violates Orlov's criterion [6]. We were, however, able to develop a 3D reconstruction procedure using a form of Inverse Monte Carlo analysis, and in particular through a Monte Carlo sampling implementation of the ISRA (Image Space Reconstruction Algorithm [7]) method. Preliminary results from this Inverse Monte Carlo approach are currently under review [8].

[1]This research was supported by US Army Medical Research and Material Command Breast Cancer Research Program Grant DAMD17-96-1-6192 and in part by the Commonwealth of Massachusetts Department of Public Health Breast Cancer Research Program Grant SC-DPH-3408-799D049.

Recently, we have been developing a very compact dual-plane PEM detector for application to image-guided biopsy, consisting of two parallel planes each with an 18 x 18 array of GSO crystals, and with each crystal 3mm x 3mm x 15mm. In the process of developing image reconstruction methods for this new device, it became apparent that the dual-plane acquisition geometry has sufficient symmetry to permit storage of a pre-calculated system response matrix in a strikingly small amount of computer memory. Consequently, this has allowed us to evaluate the merits and limitations of Monte Carlo sampling calculations as opposed to direct system matrix element calculations, by direct comparison of both techniques as applied to simulations and measurements with our new PEM device. In what follows we will present some first results from these comparative studies.

II. THEORY

We use the notation of Titterington [9], as have others. For J source pixels, the *jth* element has emission density λ_j. The measured data n_i^* is the number of coincidences recorded in the *ith* of I pairs of coincident detector elements. The conditional probability that an event emitted from source element j is assigned to projection i is given by a_{ij} (the system response matrix element). In the 3D acquisition case 3 dimensions are associated with J, while 4 dimensions are associated with I (as can readily be seen for one 2D plane in coicidence with another 2D plane).

The EM algorithm generates a sequence of estimates for each iteration, with the iterative step given by:

$$\lambda_j^{(k+1)} = \lambda_j^{(k)} \sum_{i=1}^{I} a_{ij} \frac{n_i^*}{\sum_{r=1}^{J} a_{ir} \lambda_r^{(k)}} \tag{1}$$

The iterative step for the ISRA algorithm can be written as:

$$\lambda_j^{(k+1)} = \lambda_j^{(k)} \frac{\sum_{i=1}^{I} n_i^* a_{ij}}{\sum_{i=1}^{I} a_{ij} (\sum_{r=1}^{J} a_{ir} \lambda_r^{(k)})} \tag{2}$$

In each case the forward projection step is given by

$$\sum_{r=1}^{J} a_{ir} \lambda_r^{(k)} \tag{3}$$

and the backprojection step is given by

$$\sum_{i=1}^{I} n_i^* a_{ij} \tag{4}$$

In Inverse Monte Carlo sampling, we are able to avoid explicit calculation (either on-the-fly or precalculated and stored) of the system response matrix elements but substituting a statistical estimate of the desired quantities. A Monte Carlo sampled estimate of the forward projection is straightforward, and is produced by generating events at random positions within each source voxel, with the number of events generated per voxel proportional to the activity in each voxel of the source estimate. The generated events are then propagated to where they are either detected or escape detection (i.e. "hit-or-miss"). Note that a sophisticated system model could here follow the fate of each photon pair in considerable detail, including potential attenuation and scatter effects. The Monte Carlo sampled estimate of the back-projection is also quite straightforward: a fixed number of events are generated randomly within each source voxel in turn, with the back-projection amplitude at the source voxel accumulated according to the amplitude of the line-of-response bin where each successful photon pair is detected. Note that the system response matrix element is encoded implicitly in the probability that a Monte Carlo event from source voxel j is successfully detected within projection i.

Strictly speaking, the above description of the EM and ISRA algorithms assume that all photons produced are in fact detected at some line-of-response. When Monte Carlo sampling, both the forward- and back-projection steps have arbitrary overall normalization, since only the relative probabilities are important. Therefore, one can simply set the overall number of forward-projected events in the 4D space equal to the number of source events in the 3D space after generating any desired number of forward projection sample events. Similarly, one can generate any desired number of events in the back-projection step and subsequently preserve normalization by setting the number of events in the back-projected 3D space equal to the number of events in the 4D space from which they were back-projected. If one follows this procedure, the iteration steps given above are valid.

III. METHODS

We have been evaluating the performance of Monte Carlo estimated forward- and back-projection operations with explicit matrix multiplication using pre-calculated system matrix elements. These matrix elements are calculated using the same Monte Carlo procedure which is used in the Monte Carlo estimates, and at the moment include 3D interaction points for each of the detected gamma photons (i.e. crystal attenuation and depth-of-interaction effects are included) but with only photocapture and no detector Compton scatter effects. Events are accumulated in all 4D lines of response for a given voxel, but the results are stored only for those lines-of-response which have non-zero values. When one neglects detector Compton scatter effects (but includes inter-crystal penetration and depth-of-interaction effects) this decreases the number of stored lines-of-response dramatically.

The system response is calculated for a representative column of 2 x 2 x 20 voxels, each 1.5mm x 1.5mm x 1.5mm and located near the center of a virtual 36 x 36 crystal array of 3mm x 3mm x 15mm crystals. This virtual crystal array is 4 times the size of our actual crystal array, allowing a single representative voxel at each depth to store information on the

system response matrix element for any crystal at its depth in the array (e.g. along the 40-voxel-long axis between the two detector planes). Vertical reflection symmetry is used to reduce the number of required elements by two. Translation symmetry is then used, with each matrix element checked to see whether it is still non-zero after translation to the target voxel location. This last just means checking whether the translated photon pair directions (associated with a given matrix element) each still hit the two 18 x 18 element detector arrays after translating the source voxel to a given location. In practice, one is able to calculate what range of translations in each direction will satisfy this condition, obviating the need for a explicit check after each translation and thereby speeding the algorithm execution.

Having implemented the above procedures and done some preliminary qualitative work to confirm their rough validity, we are now prepared to begin quantitative measurement of the relative speed and performance of each method. This will be particularly interesting as a function of the number of collected events, and as a function of the accuracy of the system model incorporated in each of the two approaches. To carry out this study we plan to implement procedures analogous to those others have used to evaluate 3D reconstruction algorithms applied to larger PET systems, using reasonably realistic software phantoms with a range of sizes, orientations, and contrasts. In particular, we are implementing a series of quantitative estimators of hot-spot detectability, cold-spot detectabilty, and structural accuracy [10].

IV. Discussion

We have implemented reconstruction algorithms for a pair of 18 x 18 crystal arrays used in a fixed parallel planar acquisition geometry. Note that the approach using explicit pre-calculation of the system matrix elements might also be used for larger systems if one preserves the translational symmetry. In practice, this means limiting accepted events to have lines-of-response with the top crystal no more than 18 crystals displaced from the bottom crystal in either lateral dimension. This allows for ample parallax to permit accurate imaging in the depth-of-field, while reducing randoms and scatter acceptance in a larger field-of-view device. We are currently implementing a reconfigurable array of 18 x 18 crystal modules, and we will explore application of these methods to this larger field-of-view device.

More generally, application of our method of drastically compressing the system response matrix depends upon the translational invariance (up to detector edge effects) of the system response matrix. The Monte Carlo sampling approach is not so constrained, and readily incorporates a non-repeating and largely non-zero system response matrix. Such a matrix arises when including such effects as source-dependent attenuation and scatter. For this reason, we are particularly interested in evaluating the relative capabilities of Monte Carlo sampled and explicitly calculated versions of 3D iterative reconstruction algorithms within this simple, constrained geometry.

V. Conclusion

We have implemented 3D iterative reconstruction procedures for a simple fixed dual-plane acquisition geometry, both using explicit pre-calculation of system response matrix elements and using Monte Carlo sampling techniques. The relative speed and performance of these techniques will determine their range of application as a function of event statistics and intrinsic detector system resolution.

VI. References

[1] Shepp L.A. and Vardi Y. "Maximum likelihood reconstruction in positron emission tomography" *IEEE Trans on Med. Imag.*,vol.MI-1,pp.113-122,1982.

[2] Lewitt R and Muehllehner G. "Accelerated iterative reconstruction for positron emission tomography based on the em algorithm for maximum likelihood estimation." *IEEE Trans. on Med. Imag.*,vol. MI-5.pp.16-22,1986

[3] Johnson C., Yan Y., Carson R., Martino R. and Daube-Witherspoon M. "A system for the 3D reconstruction of retracted-septa PET data using the EM algorithm." *IEEE Trans. on Med. Imag.*,vol. 42.pp.1223-1227,1995

[4] Defrise M,Kinahan P.E, Townsend D.W, Michel C, Sibomana M. and Newport D.F "Exact and approximate rebinning algorithms for 3-D PET data" *IEEE Trans. on Med. Imag.*,vol. 16,pp. 145-158,1997

[5] Worstell W. Johnson O, Kudrolli H, Zavarzin V. "First results with high-resolution PET detector modules using wavelength-shifting fibers" *IEEE Nucl. Sci. Sym. Conf. Records,Albuquerque*Cat. No. 97CH36135,1997

[6] Orlov S.S "Theory of three-dimensional image reconstruction. I Conditions for a complete set of projections." *Soviet Physics Crystallography* vol 20(4),pp.429-433,1976

[7] Daube-Witherspoon M.E and Muehllehner G, "An iterative image space reconstruction algorithm suitable for volume ECT" *IEEE Trans. on Med. Imag.*,vol. MI-5,pp.61-66,1986

[8] Kudrolli H., Worstell W., Zavarzin V. "An inverse Monte Carlo algorithm for 3-D PET Image Reconstruction" Poster M6-67, IEEE Conference on Nuclear Science and Medical Imaging, Toronto 1998. Submitted to conference proceedings.

[9] Titterington D.M. "On the Iterative Image Space Reconstruction Algorithm for ECT" *IEEE Trans. on Med. Imag.*,vol. MI-6,pp.52-56,1987

[10] Furuie S.S, Herman G.T, Narayan T.K, Kinahan P.E, Karp J.S, Lewitt R.M and Matej S. "A methodology for testing statistically significant differences between fully 3D PET reconstruction algorithms" *Phys. Med.Biol.*,vol. 39,pp.341-354,1994

Quantitative Evaluation of an Inverse Monte Carlo procedure for 3-D PET Image Reconstruction [1]

H.Kudrolli[2] , W.Worstell[2] and V.Zavarzin[3]
[2]Boston University Physics Department and Center for Photons. 590 Commonwealth Avenue, Boston, MA 02215
[3]Tomotronics, Inc. 5 Snake Brook Road. Wayland, MA 01778-5013.

Abstract

We have developed a three dimensional (3D) reconstruction procedure for positron emission tomography (PET) based on Inverse Monte Carlo analysis (IMC). This procedure uses Monte Carlo techniques to simulate the process of photon emission and detection from a hypothesized source distribution. A Monte Carlo simulation of a given source/detector system implicitly contains the information in the system response matrix. By generating Monte Carlo events one can sample from the system matrix to estimate forward or backward projection operations. We have explored this approach in the context of the image space reconstruction algorithm (ISRA) [2] where the system matrix is too large to be calculated and stored practically.

This technique was tested on a series of software phantoms and also from data taken from high resolution PET scanners [1]. The current work involves quantitatively evaluating the performance of the technique, using the methodology suggested by Furie et al [3, 4]. Reconstruction parameters, like the number of Monte Carlo events to be generated per iterations,the initial source hypothesis, and the stopping criteria, will be optimized using this methodology. Performance of the technique will be evaluated according to figures of merit associated with structural accuracy, hot spot detectability and cold spot detectability.

I. INTRODUCTION

The recent trend in operating PET detectors in three-dimensional mode, to achieve higher sensitivity, has heightened interest in 3D image reconstruction algorithms. The requirements for such algorithms is that they have to be quantitatively accurate, and have fast reconstruction times. The 3DRP algorithm proposed by Kinahan and Rogers [5] is currently commonly implemented on commercial PET scanners. This algorithm is fast, robust and has good image contrast, but suffers from poor noise properties and treatment of statistical data. Statistical methods, like the maximum likelihood - expectation maximization (ML-EM) [6, 7, 8], penalized weighted least squares (PWLS) [9] and Bayesian reconstruction procedures[10], give improvements in image quality at increased computational cost. These set of algorithms are iterative, and require explicit calculation of the system response matrix. This matrix gives the probability that a photon emitted from a certain source element will be detected in a particular detector line of response. This probability matrix is usually much too large to store in memory and has to be either stored on disk or calculated on the fly. Several groups have used symmetries and sparseness of this matrix to be able to store it in memory [10]. The ordered subsets (OS-EM) algorithm [11] uses subsets of the data to speed up the iterations but the reconstruction times for 3D mode are still quite large. Approximate rebinning algorithms like the FORE algorithm rebin data into set of 2D slices [12]; the rebinned slices can be reconstructed using filtered backprojection or ML-EM, OS-EM or WLS methods. These algorithms are computationally fast but the accuracy of the reconstructed images is limited by the approximations implicit in the line integral model and the non-Poisson statistical properties of the resultant slice data [13].

Our interest in image reconstruction arises from development of a novel detector with dual plane acquisition geometry [14]. For this detector, the incomplete set of projections excludes the possibility of using Fourier filtered backprojection techniques since the geometry does not satisfy Orlov's criterion [15]. Iterative algorithms which are not restricted by device geometry are a possibility but the computational burden associated with explicitly calculating the system response function makes them difficult if not impractical.

Monte Carlo methods for solving the inverse problem in ECT has been previously reported by other groups [16]. This method generally uses Monte Carlo methods to calculate the system response matrix, taking into account attenuation and scatter of the gamma rays. The ML-EM algorithm is then used to solve for the source distribution. Monte-Carlo methods have also been used in PET to study the effects of attenuation and scatter as they provide a natural framework for incorporation of detector response functions, and the effects of attenuation and other sources of systematic errors.

Our approach may be distinguished from these approaches, in that, it uses Monte Carlo generation of events to model the emission and detection of photons from a hypothesized source distribution within each iteration, and thus avoids the explicit calculation of the system response matrix.

II. THEORY

Our first application of Inverse Monte Carlo procedures has been in the context of the 3D ISRA algorithm. This algorithm introduced the concept of storing data as backprojection

[1]This research was supported by US Army Medical Research and Material Command Breast Cancer Research Program Grant DAMD17-96-1-6192 and in part by the Commonwealth of Massachusetts Department of Public Health Breast Cancer Research Program Grant SC-DPH-3408-799D049.

array, thereby compressing the large and sometimes sparsely populated projection matrix into a more compact data image matrix. In this algorithm, the update to the source hypothesis is done by comparing, the backprojection of the data and the backprojection of projections from the source hypothesis. Titterington [17] showed that this algorithm converges to the least squares estimate, as long as the source elements are strictly positive. Using his notation; for J source pixels, the *jth* element has emission density λ_j. The measured data $n_i{}^*$ is the number of coincidences counted in the *ith* of I pairs of coincident detector elements. The conditional probability that an event emitted from pixel j is assigned to projection i is given by a_{ij}. The iterative step for the ISRA algorithm can be written as

$$\lambda_j{}^{(k+1)} = \lambda_j{}^{(k)} \frac{\sum_{i=1}^{I} n_i{}^* a_{ij}}{\sum_{i=1}^{I} a_{ij} (\sum_{r=1}^{J} a_{ir} \lambda_r{}^{(k)})} \quad (1)$$

where the forward projection step is given by

$$\sum_{r=1}^{J} a_{ir} \lambda_r{}^{(k)} \quad (2)$$

and the backprojection step is given by

$$\sum_{i=1}^{I} n_i{}^* a_{ij} \quad (3)$$

The IMC technique replaces the explicit forward projection calculation in ISRA, by Monte Carlo generation of events according to the hypothesized source distribution. Photon pairs are generated at random positions within the source voxels, with the number of photon pairs generated per voxel proportional to the hypothesized source intensity at that voxel.These photon pairs are given a random direction and traced to determine where and whether they hit the detector. An elaborate source and system response model could contain attenuation and scatter in the source, as well as details of the detector response properties like resolution, scatter and attenuation in the detector elements. In practice, we have explored a very simple system model containing only the basic detector geometry.

The events that hit the detector are backprojected. In formal terms backprojection is the convolution of the system response matrix with the projection matrix as shown in equation 3. The system response matrix element a_{ij} can be approximated by the length of the intersection of the *ith* line with the *jth* pixel [18]. Hence the backprojection operation can be approximated as, the accumulation according to the chord length by which each cubic voxel along a line of response is intercepted. [19].

Like in ISRA, the ratio the backprojection of the data and the backprojection of the simulated data, for a voxel element, is used to update the image voxel element.

The backprojection of the data into image space is used as the initial source estimate during the first iteration. In the following iterations, the number of events generated from a voxel is updated (multiplied) by, the ratio between the backprojection of the data to the backprojection of the Monte Carlo generated "pseudo-data"at that voxel. The pseudo-data events are similarly projected to find where they hit the detector and then backprojected.If the simulated backprojection at the source voxel is less than the measured backprojection at that voxel, then more pseudo-data events are generated. Conversely, if the simulated backprojection is more than the measured backprojection then, the pseudo-data events are removed.

III. Preliminary Results

A simulated Hoffman brain phantom [20] with 1 mm spatial resolution; neglecting attenuation and scatter, was reconstructed using the IMC algorithm. The detector geometry used for this purpose was that of the HEAD PENN-PET detector. The HEAD PENN-PET scanner is a volume-imaging PET scanner without inter-plane septa, with high spatial resolution and sensitivity [21]. 75 million events were simulated from the phantom and the data was stored as a backprojection array. The images shown in Figure 1 were reconstructed simulating 350 million events, using 4 mm^3 voxel size, with the image array size of 60 X 60 X 48. The algorithm was implemented on a SGI/Cray Origin2 Series parallel computer using 8 processors. The reconstruction time required for this implementation was about 5 minutes for 25 iterations .

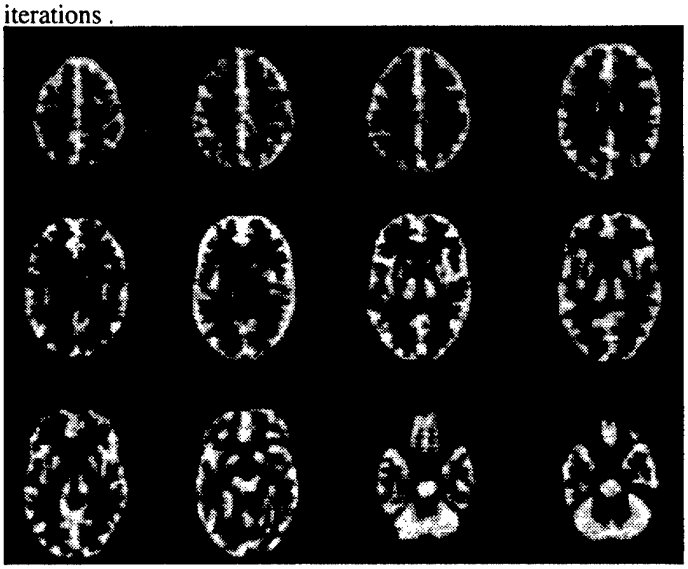

Figure 1: Simulated Hoffman Brain Phantom using 4 mm^3 voxel size and 60 X 60 X 48 image array size ; using 25 iterations and simulation 350 million events

The algorithm was also applied to Hoffman brain data acquired by the HEAD PENN-PET data. The total number of attenuation corrected events in this data were about 800 million. Using 4 mm size voxels the image (60 X60 48) was reconstructed in 25 iterations within 15 minutes while simulating 3 billion events [1]. The images from this reconstruction are shown in Figure 2. In this implementation the simulated events are traced to find where they hit the

detector and accumulated. Backprojection is done once per iteration after all the simulated events are generated. Using symmetries in the image array the backprojection is sped by an order of magnitude. Hence reconstruction time does not scale up linearly with increased number of simulated events.

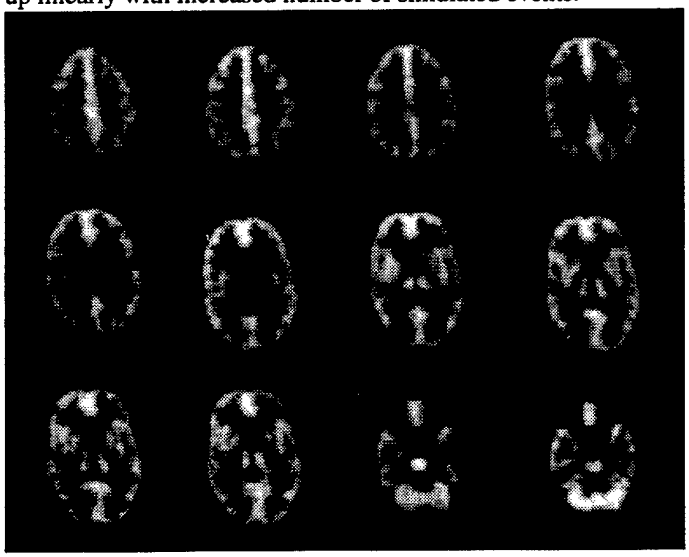

Figure 2: Hoffman Brain Phantom using 4 mm^3 voxel size and 60 X60 X48 array image size; using 25 iterations and simulating 3 billion events. Data was acquired by HEAD PENN-PET detector

IV. Discussion

The images shown above demonstrate the feasibility of using Inverse Monte Carlo for image reconstruction. The next task, which is currently underway, is to quantitatively evaluate the performance of this algorithm. To do so we are using the methodology proposed by the Medical Image Processing Group (MIPG) at the University of Pennsylvania [3, 4]. They have developed a software package called EVAL3DPET [22] which are a set of programs designed to statistically evaluate 3D PET reconstruction algorithms. This software is capable of generating phantom and projection data based on a realistic 3D PET scanner model. The phantoms are random samples from a statistically described ensemble of 3D images with 69 ellipsoid features with varying activity and sizes. The projection data takes into account detector field-of-view blurring and a realistic 3D PET noise model.

The images reconstructed from this phantom can be evaluated for structural accuracy, hot spot detectabilty and cold spot detectabilty. The evaluation program also calculates a training figure-of-merit,that can be used for optimizing the free parameters of the reconstruction techniques. The parameters of the IMC algorithm that we would like to optimize are the total number of events to simulate, the number of events to simulate per iteration, the number of iterations or the stopping criteria and also, the choice of our first estimate.

Increasing the number of events generated reduces statistical fluctuations of the simulated data, and yields better images. Generating a large number of events, however, increases the reconstruction time, without appreciably improving image quality. We have worked with a stopping criteria that the number of events generated is about 10 times the number of events detected. We have observed empirically that the image quality does not improve significantly for more events generated.

There are various choices for the first estimate of the source distribution , such as a uniform field or an image formed from some earlier iteration or other algorithm .The backprojection of the data can also be used as the first estimate, and it has been observed that this is a good starting point. Using the training figures-of-merit we will form the basis of selecting the best starting point to give fast, accurate images of 3D PET data.

V. Conclusion

We have explored the possibility using Inverse Monte Carlo methods for image reconstruction and applied it to digital phantoms, as well as, data from 3D PET detectors. The algorithm is shown to give qualitatively accurate images of complex phantoms. This work will present quantitative evaluation of the algorithm using figures of merit based on structural accuracy, hot spot detectabilty and cold spot detectabilty.

VI. Acknowledgments

The authors would like to thank Dr. Joel Karp and Dr. Lars-Eric Adams, from University of Pennsylvania for providing us with the data for the Hoffman Brain phantom, and also for their helpful suggestions. We would also like to thank Dr. E. J. Hoffman for providing us the digital version of the Hoffman brain phantom.

VII. References

[1] Kudrolli H., Worstell W., Zavarzin V. "An inverse Monte Carlo algorithm for 3-D PET Image Reconstruction" Poster M6-67, IEEE Conference on Nuclear Science and Medical Imaging, Toronto 1998. Submitted to conference proceedings.

[2] Daube-Witherspoon M.E and Muehllehner G, "An iterative image space reconstruction algorithm suitable for volume ECT" *IEEE Trans. on Med. Imag.*,vol. MI-5,pp.61-66,1986

[3] Furuie S.S, Herman G.T, Narayan T.K, Kinahan P.E, Karp J.S, Lewitt R.M and Matej S. "A methodology for testing statistically significant differences between fully 3D PET reconstruction algorithms" *Phys. Med.Biol.*,vol. 39,pp.341-354,1994

[4] Matej S, Herman G.T, Narayan T.K,Furuie S.S, Lewitt R.M and Kinahan P.E. "Evaluation of task oriented performance of several fully 3D PET reconstruction algorithms." *Phys. Med.Biol.*,vol. 39,pp.355-367,1994

[5] Kinahan P.E and Rogers J.G "Analytic three-dimensional image reconstruction using all detected events" *IEEE Trans. on Nucl. Sci.*,vol. 36,pp.964-968,1990

[6] Shepp L.A. and Vardi Y. "Maximum likelihood reconstruction in positron emission tomography" *IEEE Trans on Med. Imag.*,vol.MI-1,pp.113-122,1982.

[7] Lange K. and Carson R. "EM reconstruction algorithms for emission and transmission tomography." *J.Comput. Assist.Tomography.*,vol.8,pp.306-316,1984

[8] Lewitt R and Muehllehner G. "Accelerated iterative reconstruction for positron emission tomography based on the em algorithm for maximum likelihood estimation." *IEEE Trans. on Med. Imag.*,vol. MI-5.pp.16-22,1986

[9] Fessler J.A. "Penalized weighted least-squares image reconstruction for positron emission tomography" *IEEE Trans. on Med. Imag.*,vol. 13,pp.290-300,1994

[10] Qi J, Leahy R.M, Hsu C, Farquhar T.H, Cherry S.R "Fully 3D Bayesian image reconstruction for the ECAT EXACT HR+" *IEEE Trans. on Nucl. Sci.*,vol. 45,pp.1096-1103,1998

[11] Hudson H.M. and Larkin R.S. "Accelerated image reconstruction using ordered subsets of projection data" *IEEE Trans. on Med. Imag.*,vol. MI-13,pp.601-609,1994

[12] Defrise M,Kinahan P.E, Townsend D.W, Michel C, Sibomana M. and Newport D.F "Exact and approximate rebinning algorithms for 3-D PET data" *IEEE Trans. on Med. Imag.*,vol. 16,pp. 145-158,1997

[13] Comtat C.,Kinahan P.E.,Defrise M.,Michel C.,Townsend D.W. "Fast reconstruction of 3D PET data with Accurate Statistical Modeling" *IEEE Trans. on Nucl. Sci.*,vol. 45,pp.1083-1089,1998

[14] Worstell W. Johnson O, Kudrolli H, Zavarzin V. "First results with high-resolution PET detector modules using wavelength-shifting fibers" *IEEE Nucl. Sci. Sym. Conf. Records,Albuquerque*Cat. No. 97CH36135,1997

[15] Orlov S.S "Theory of three-dimensional image reconstruction. I Conditions for a complete set of projections." *Soviet Physics Crystallography* vol 20(4),pp.429-433,1976

[16] Floyd C.S and Jaszczak R.J, "Inverse Monte Carlo: A unified reconstruction algorithm for SPECT." *IEEE Trans. on Nucl. Sci.*,vol. 32,pp.779-785,1985

[17] Titterington D.M. "On the Iterative Image Space Reconstruction Algorithm for ECT" *IEEE Trans. on Med. Imag.*,vol. MI-6,pp.52-56,1987

[18] Vardi Y., Shepp L.A. and Kaufman L. "A statistical model for positron emission tomography" *J. Amer. Statist. Ass.*, vol.80, no.389,pp. 8-20,1985

[19] Barresi S, Bollini D, and Del Guerra A, "Use of a transputer system for fast 3-D image reconstruction in 3-D PET" *IEEE Trans. on Nucl. Sci.*,vol. 37,pp.812-816,1990

[20] Hoffman EJ, Cutler PD, Digby WM, Mazziotta JC. "3-D Phantom to Simulate Cerebral Blood Flow and Metabolic Images for PET." *IEEE Trans. Nucl. Sci.*,vol. 37,pp. 616-620, 1990.).

[21] Karp J.S, Freifelder R, Geagan M.J, Muehllehner G, Kinahan P.E, Lewitt R.M Shao L. "Three-dimensional imaging characteristics of the HEAD PENN-PET scanner" *Jour. of Nucl. Med.*,vol. 38, No. 4,pp. 636-642,1997

[22] EVAL3DPET "Programs for evaluation of 3D PET reconstruction algorithms." *http://www.mipg.upenn.edu/ Vnews/eval3dpet/index.html*

CONCLUSIONS

Our principal accomplishment has been the successful construction and imaging characterization of a 12cm x 12cm field-of-view PEM instrument. Performance measurements and other outcomes for this preliminary device are detailed below by category.

1) Spatial Resolution and Uniformity:

We have obtained 2mm FWHM (Full Width at Half Maximum) spatial resolution in imaging a point-like source. Quantitatively uniform sensitivity over a large spatial range was also. Spatial calibration of the detector was straightforward when imaging a point source, and 3-4mm FWHM resolution was obtainable with no calibration constants at all. Boundary effects between adjacent fiber ribbons were found to be minimal, and determination of interaction coordinates was robust and unambiguous because of the substantial fiber light yield (averaging 8 photoelectrons/511 keV interaction) and because of the intrinsic linearity of interaction position measurement through local light collection by fibers. The coordinates obtained were also accurate to the very edge of each prototype detector, as opposed to the Anger coordinates which were quite distorted near each edge.

2) Light Yield:

We have obtained an average of 8 photoelectrons at the fiber readout for 1mm fibers and roughly 200 photoelectrons at the Anger PMT readout, using CsI(Na) crystals. The Anger light yield was low partially because of incomplete photocathode coverage by four 2" round PMTs, and we have purchased and obtained 60mm square PMTs for successor modules. Another cause is the relatively low PMT quantum efficiency for green wave-shifted light.

3) Energy Resolution:

We have obtained 20% energy resolution FWHM, after correction for nonuniformity in the Anger PMT light collection across the module (this calibration is straightforward, given the fiber-derived event coordinates and the 511 keV photopeak). Of this, about 15% FWHM is intrinsic nonuniformity and about 15% is due to our limited photostatistics (these effects add in quadrature). Therefore, we anticipate a future energy resolution of about 15% FWHM, assuming 400 photoelectrons/511 keV collection. This should easily be adequate for clinical scatter rejection.

4) Timing Resolution:

We have obtained 50ns FWHM timing resolution for CsI(Na) modules by using a second low threshold on the Anger sums in addition to the threshold used for energy'trigger discrimination. This is in agreement with the decay time of the CsI(Na) and the results from computer simulation of the best timing achievable as a function of integration time and threshold level.

5) Optoelectronics and Data Acquisition Electronics:

We have developed a high-performance, low-cost, and compact data acquisition system suitable for high-rate PET data acquisition with a portable instrument.

6) Image Reconstruction and Analysis:

Reconstruction algorithms, including background subtraction and attenuation/scatter corrections, is being carried out with a novel iterative reconstruction algorithm which we have developed. Iterative reconstruction permits 3d limited-angle tomography, such as is our case with two modules which do not completely surround the region of interest (i.e. a breast or axillary tails).

BIBLIOGRAPHY

1) Grigoriev D, Johnson O, Worstell W, and Zavarzin V, "Characterization of a new multianode PMT for low-level optical fiber readout", IEEE Transactions in Nuclear Science, 1997, pp.638-641.

2) Zavarzin V and Earle W, "A 500K Event/Sec ADC System with High-Speed Buffered PCI Interface", IEEE Nuclear Science Symposium Conference Proceeding, 1998.

3) Worstell W, Johnson O, and Zavarzin V, "Development of a High-Resolution PET Detector using LSO and Wavelength-shifting Fibers", IEEE Medical Imaging Conference Proceedings, 1996.

4) Worstell W, Johnson O, Kudrolli O, and Zavarzin V, "First Results with High-Resolution PET Detector Modules using Wavelength-Shifting Fibers", accepted for publication in 1998 IEEE Transactions in Medical Imaging.

5) Kudrolli H, Worstell W, and Zavarzin V,"An Inverse Monte Carlo Algorithm for 3-D PET Image Reconstruction", IEEE Medical Imaging Conference Proceedings, 1998.

PERSONNEL SUPPORTED

William A. Worstell
Assistant Professor of Physics
Boston University Physics Department
Partial support of summer salary

Valery G. Zavarzin
Research Associate
Boston University Physics Department
Partial support of academic year salary

Haris A. Kudrolli
Research Assistant
Boston University Physics Department
Partial support of academic year stipend